

1 Article

2 Effect of Current Density Ramping on the Growth Rate and 3 Structure of AA2024-T3

4 Peter Totaro^{1,2} ORCID 0000-0003-4923-5866, Boris Khusid^{1,*} ORCID: 0000-0002-8604-1051

5 ¹ Otto H. York Department of Chemical and Materials Engineering, New Jersey Institute of Technology,
6 University Heights, Newark, NJ 07102, USA; khusid@njit.edu

7 ² Aerotech Processing Solutions, 57 Wood St., Paterson, NJ, 07524, USA; ptotaro@aerotechprocessing.com

8 * Correspondence: khusid@njit.edu; Tel.: +1-973-596-3316

9 **Abstract:** The presented study successfully demonstrated advantages of multistep anodization of
10 AA2024 – T3. Coating properties and morphology were studied in detail for five anodization
11 processes: a conventional Base process with a constant applied current density and processes with
12 current density applied in one (OS1 and OS2) and five (MS1 and MS2) steps at different
13 magnitudes during the ramp period. Due to lower oxygen infusion, processes MS1 and MS2
14 produced a more intact coating with reduced porosity and enhanced abrasion resistance and
15 hardness. The presented results clearly demonstrate that starting anodizing processes at a low
16 voltage and then slowly ramping current density will form more aluminum rich coatings with
17 enhanced properties in a shorter period.

18 **Citation:** Totaro, P.; Khusid, B.;
19 Effect of Current Density Ramping
20 on the Growth Rate and Structure of
21 AA2024-T3. *Materials* **2022**, *15*, x.
<https://doi.org/10.3390/xxxxx>

Academic Editor: Firstname Last-
name

Received: date

Accepted: date

Published: date

Keywords: Aerospace Aluminum-Copper Alloys, Anodizing, Ramping, Intermetallics, Current
Density

1. Introduction

The use of 2000 series aluminum alloys in aerospace applications requires the application of surface treatments to improve the corrosion resistance and mechanical properties of the product surface [1]. Surface modifications such as anodization, friction stir processing, and plasma electrolytic oxidation are needed to improve mechanical properties such as hardness, wear and corrosion resistance, and tribological properties [2-4]. Anodization is one of the most utilized methods to enhance the mechanical properties of aluminum alloys [5-8].

23 **Publisher's Note:** MDPI stays
24 neutral with regard to jurisdictional
25 claims in published maps and
26 institutional affiliations.



27 **Copyright:** © 2022 by the authors.
28 Submitted for possible open access
29 publication under the terms and
conditions of the Creative Commons
Attribution (CC BY) license (<https://creativecommons.org/licenses/by/4.0/>).

6

30 The presence of copper, a key alloying element, is used to form precipitates in the
31 bulk by thermal ageing treatment [9,10] to enhance the alloy mechanical strength,
32 fracture toughness, and fatigue properties [11-13]. Unfortunately, a difference between
33 electrochemical potential of the aluminum alloy matrix and intermetallics promotes
34 galvanic reactions that render the surface highly electro active [13-15]. These
35 electrochemical differences lead to uneven growth and burning during anodization due
36 to a spatially non-uniform distribution of electric current [11,13-19]. This condition is
37 exacerbated if higher voltages and current densities are applied [11,13-19]. The presence
38 of copper enhances local parasitic reactions that reduce faradaic efficiency of anodization
39 and produce a flawed porous oxide layer [13,20-23].

40 The research on anodization of aluminum-copper alloys generally focuses on
41 evaluating the influence of complex electrolyte baths, where addition of different acids
42 such as malonic [5], carboxylic [24] fluorozirconic [25], citric [26], boric [27], and adipic
43 [28] acids, are mixed with sulfuric acid to enhance the mechanical properties,
44 morphology and reduce processing issues [24-30]. Alternatively, industrial Types II and
45 III anodization processes of aluminum alloys require the use of sulfuric acid bath, and
46 the application of electrolyte blends is limited [1,31-32]. Temperature and applied
47 current/voltage are the basic process variables which can be manipulated in industry to
48 improve the anodic coating [5]. However, variation of temperature is limited to the
49 process of Type III, hard anodization. Therefore, the influence of applied current/voltage
50 on the morphology and properties of anodic coatings are a subject of major interest for
51 the industrial Type II anodizing process [1,31-32].

52 Anodizing current/potential influences the coating structure and properties as
53 porosity and pore size are directly proportional to the magnitude. [33-35]. Anodization
54 at fixed voltages promotes large current densities and high local heating at the
55 beginning of the process that generates burning and reduces the film growth. This
56 renders the coating properties unsuitable for a wide range of applications due to the
57 presence of soft, porous coating and conical asperities [13,21,27]. The concept of ramping
58 in anodization is to gradually raise the current density at the beginning of the process to
59 prevent overpotential spikes. It has been recognized that changing the current density
60 during the process has positive effects by increasing the heat dissipation and
61 deoxygenation at the surface of the forming anodic coating [13,19,36-40]. Pulse
62 anodization, an example of varying current density, [13] was observed to improve
63 coating properties of AA 2024-T3, but the proposed process requires expensive
64 equipment that is not readily available in an industrial setting.

65 Our previous work [15] revealed the advantages of multistep anodization of AA
66 7075 – T6, (5.6–6.1% Zn, 2.1–2.5% Mg, 1.2–1.6% Cu), in a standard Type II sulfuric acid
67 electrolyte. The composition of AA2024 – T3, (4.3–4.5% Cu, 0.5–0.6% Mn, 1.3–1.5% Mg),
68 is much different, and the difference in composition changes electrochemical behavior. It
69 is well established that a difference in the size and mobility between copper and zinc

ions changes their diffusion patterns and alters the formation of an anodic coating on these alloys [14,16,36,41]. Zinc ions accumulate at the anodic oxide/aluminum interface, while copper ions are found throughout the anodic coating and on the specimen surface [16,36,41]. The presence of zinc and copper are known to create defects in the anodic coating that are detrimental for the coating morphology and properties. Since AA7075 – T6 and AA2024 – T3 require different anodizing processes [14,22,31,42-45], it is difficult to predict whether advantages of stepwise anodization observed for AA7075 – T6 would also benefit AA2024 – T3.

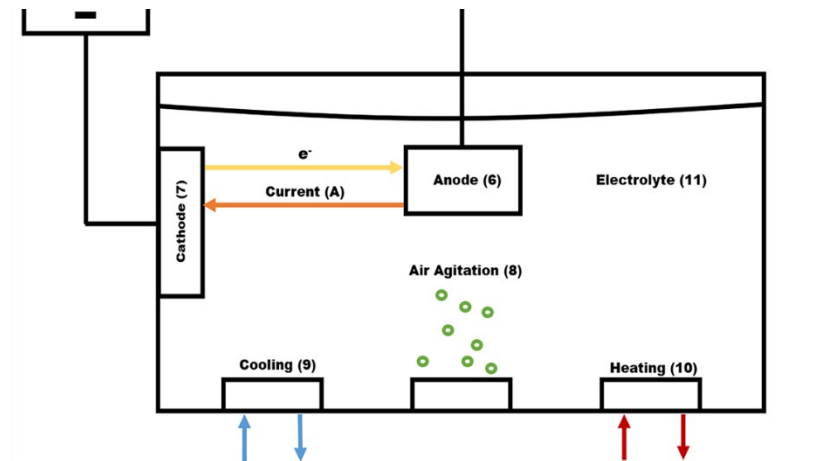
The present paper aims to study the influence of applying current density in multiple steps during the ramping stage on the morphology and performance properties of an anodic coating formed on AA 2024-T3 in a sulfuric acid bath. The results presented in this paper on the microstructure, growth rate and service performance of a coating formed on AA2024 – T3 show that raising the current density in five steps improves the overall process in terms of consistency, performance, and efficiency compared to a constant current anodization. We expect that a better understanding of the impact of multistep anodization on the coating properties of AA2024 – T3 taken together with data on AA7075 – T6 [15] would lay out the framework for the development of more efficient anodization processes on aluminum alloys.

2. Materials and Methods

2.1 Anodizing Process

Anodization was performed in an electrochemical cell, Fig. 1, in which voltage, amperage, and transferred charge are controlled with the module UPC 5000 RC-2 D P18/1000-24VN-C0, American Plating Power LLC, Florida. The UPC 5000 module was connected by a 50-mA shunt to the DC rectifier (American Plating Power LLC, Florida) (1). The electrochemical cell consists of a polyvinylchloride tank, where the electrolyte temperature was controlled externally by a two-output/input controller.

12



99

100

101

102

Figure 1. Anodizing system: 1) Power supply, 2) Voltmeter, 3) Ammeter, 4) Amp-Hour meter, 5) Computer, 6) Anode, 7) Cathode, 8) Air agitation, 9) Cooling system, 10) Heating system, 11) Electrolytic solution.

103

104

105

106

107

108

Air agitation was performed utilizing constant low-pressure air (8). The cathodes (7) and the rack that suspended the anode (6) into the electrolyte were made of 6063 aluminum extruded bars. The cathode/anode area was kept at a 1:1 ratio measuring a total area of 0.097 m^2 . The area of each load is 0.097 m^2 with 0.0485 m^2 being the rack area and 0.0485 m^2 being the part area. One cathode was mounted on each side of the tank for even distribution of an electric current.

109

110

111

Experiments were carried out on specimens of AA2024 – T3 provided by Anacon 1st Choice, 425 W LA Cadena Riverside, California. The alloy bulk chemical composition given by the manufacturer is reported in Table 1.

112

113

114

115

116

Table 1. Composition, wt. % of AA2024 – T3 specimens provided by Anacon 1st Choice, 425 W LA Cadena. Riverside, California. The first row is the bulk composition given by the manufacturer. Secondary and Backscattered SEM images at $30,000\times$ were obtained using 10 kV under LED and the height of the specimen stage, WD, of 10.0 mm to observe the surface morphology and measure the local composition with EDS, see Fig. 7(a-b).

15

Elements (wt. %)	Al	Cu	Mg	Mn	Fe	Zn	Si	O
Manufacturer Data	92.8	4.8	1.4	0.6	0.2	0.1	0.1	-
EDS/Non - Particle Region	80.2 ± 7.4	5.7 ± 1.1	4.4 ± 0.9	1.1 ± 0.7	1.0 ± 0.8	0.7 ± 0.2	0.5 ± 0.1	6.4 ± 3.8
EDS/ Particle Region	65.2 ± 6.3	12.3 ± 4.7	6.2 ± 3.2	2.5 ± 1.6	2.4 ± 1.1	0.4 ± 0.1	0.4 ± 0.1	10.6 ± 4.6

117

118

119

120

121

122

123

124

125

126

127

128

129

130

131

132

133

134

135

All specimens were purchased as 10 × 10 × 0.16 cm squares with a hole of 0.64 cm diameter in the middle. Specimens were then further cut to 2.54 × 2.54 × 0.16 cm squares using a diamond blade and a portable bandsaw and then deburred to reduce sharp edges. Prior to chemical processing, all specimens, anodized and non-anodized, were cleaned with reagent-grade acetone before racking to remove glue, ink, and other surface impurities. Specimens were chemically processed using an alkaline cleaner, NaOH, for 10 mins, followed by a pickling process in a ferric sulfate/nitric acid bath for 5 mins. Specimens were rinsed by deionized (DI) water in between each chemical step. Untreated specimens went directly to the drying step after the cleaning process. After the preparation steps, specimens were anodized at room temperature, 20°C, for 30 mins. The electrolyte (11) consisted of sulfuric acid, 180 g/L. After anodization, the specimens were cleaned in DI water and air dried.

136

137

138

139

Five anodization processes listed in Table 2 as Base, OS1, OS2, MS1 and MS2 were studied. "Base" is a conventional process with a constant electric current density; letters "OS" and "MS" mean, respectively, one-step and five-step ramping of an applied current density. Numbers "1" and "2" indicate, respectively, low, and medium current densities in ramping steps. Electric current densities applied in these processes, Table 2, span a typical range of current densities utilized in industry.

Table 2. Anodizing processes designed for experiments: a conventional Base process with a constant applied current density and processes with current density applied in one (OS1 and OS2) and five (MS1 and MS2) steps at different magnitudes during the ramp period. The expected values of transferred electric charge computed with the use of Eq. 1 and Eq. 2.

Process	Mins	Current Density, A/m ²	Charge, C	Amperage, A
Base	30	180	30600	17
OS1	10	32	1800	3
	20	180	20400	17
OS2	10	111	6600	11
	20	180	20400	17
MS1	2	32	360	3
	2	40	480	4
	2	49	600	5

18

	2	57	600	5
	2	65	720	6
	20	180	20400	17
MS2	2	32	360	3
	2	64	720	6
	2	95	1080	9
	2	126	1440	12
	2	158	1800	15
	20	180	20400	17

140

141

142

143

144

145

146

147

148

149

150

151

152

153

154

155

Stepwise processes were designed to explore the influence of varying the number of steps and current density during the ramp on the coating morphology and properties. In the stepwise processes, (OS1, OS2, MS1 and MS2), ramping of an applied current density was conducted for 10 mins and the remaining 20-min period was carried out at a constant current (Table 2). The Base process, considered as the baseline for comparison, did not utilize a ramp. Anodic samples for testing were taken during 3 stages of the process. The samples were taken at 2-min intervals up to and including 10 mins, and at the end of the process, 30 mins. The Base process was included in the testing to study the effects of constant high current density in the same 10-min period.

The anodization process was designed to have the same electric charge passing through the system during the final stage of processing (20 mins) [15]. This task was implemented to show the impact of stepwise anodization during the ramp phase of processes listed in Table 2. An electric current was calculated with the use of Eq. (1) and the expected values of electric charge for the designed processes of anodization were computed with the use of Eq. (2)

$$A = X \cdot J, \quad (1)$$

156

157

where A is the current in amperes, X is the area in m^2 , and J is the current density in A/m^2 .

$$C = 60 \cdot A \cdot M, \quad (2)$$

158

159

160

161

where C is Coulomb = A·sec, A is in amperes and M is the period in minutes during which a certain current is applied, 60 is the conversion factor from minutes to seconds. Computed values of the anodizing electric current and the expected transferred electric charge for Base, OS1, OS2, MS1 and MS2 processes are summarized in Table 2.

21

2.2 Characterization techniques

i) The values of amperage, transferred electric charge, and actual voltage was measured using module UPC 5000 calibrated to NIST (+/- 0.1 V, 0.1 A). The presented voltage, amperage, and charge are values averaged over three repeated anodizing processes.

ii) Measurements of the coating thickness were conducted after air drying anodized specimens at temperature of 20.0 °C for 1 hour (± 5 mins). The coating thickness was measured using an Eddy current meter (Positector 6000, Deflesko, New York). Four thickness readings were taken for every anodized specimen and the presented result is averaged over three repeated anodizing processes.

iii) Test panels for abrasion resistance were conditioned at 46.2 % relative humidity (RH) and 23.7 °C for 48 hours before testing. After conditioning, panels were weighed to the nearest ± 0.0001 g with an Ohaus digital balance (PA224, Ohaus, New Jersey). After weighing, panels were positioned on the Taber abraser and allowed to re- condition for 2 hours and then tested in the same conditions. Abrasion CS-17 wheels (CS-17, Taber, New York) with a 1000 g load were used to abrade the surface of the specimen. Following the American Society for Testing and Materials (ASTM) D4060 standard, the Taber abraser was placed inside the SCCH high humidity chamber to condition the testing environment. Abrasion resistance was tested on two anodized specimens per process and the presented result is averaged over three repeated anodizing processes.

iv) Micro-hardness of anodized specimens was measured by a digital Vickers tester (Durascan 50, Struers, Ohio) with a 10 g load for 15 s. Micro-hardness readings were tested on two anodized specimens per process and the presented result is averaged over three repeated anodizing processes.

v) Acid dissolution tests of the 7.62 x 7.62 cm anodized specimens were carried out in accordance with ASTM B680 - 80 (2019) and ASTM B 137 - 95 (2014) specifications. A specimen was immersed for 15 ± 0.1 min in the stirred acid test solution maintained at a temperature of 38 ± 1 °C. Two tests were performed using the following solution: 35 ± 0.5 mL of Orthophosphoric acid of 85 mass %, 20 ± 0.5 g of Chromic acid anhydride (CrO₃) and balance to 1000 ml of deionized water. Mass loss in mg/dm² was calculated using Eq. (3) [46] in accordance with ASTM B680 - 80 (2019):

$$\text{Mass Loss, mg/dm}^2 = \frac{(W_1 - W_2)}{A} \quad (3)$$

Total coating dissolved in the test was calculated using Eq. (4) [46] in accordance with both ASTM B 137 - 95 (2014) and ASTM B680 - 80 (2019):

$$\text{Coating Dissolved in Test, \%} = \frac{(W_1 - W_2)}{(W_1 - W_3)} \times 100 \quad (4)$$

162

163

164

165

166

167

168

169

170

171

172

173

174

175

176

177

178

179

180

181

182

183

184

185

186

187

188

189

190

191

192

193

194

24

195 where, W_1 is the initial weight, mg, W_2 is the weight after testing, mg, W_3 is the weight
196 after all coating was removed, mg, and A , is area in dm^2 .

197 vi) Salt Spray (Fog) Testing is an accelerated corrosion test used to evaluate the
198 corrosion resistance of metals and coated metals [47]. This test method, ASTM B117, has
199 been approved for use by agencies of the U.S. Department of Defense and is widely used
200 in testing of anodic coatings [30, 47-51]. Corrosion resistance testing by Salt Spray was
201 conducted using $10 \times 10 \times 0.16$ cm test panels that were anodized for 10 and 30 mins and
202 sealed in Anodal MS-1 New (Reliant Aluminum Products, North Carolina) for 20 mins
203 at 90°C . One anodized specimen was tested for each anodizing process and the
204 presented result is averaged over three repeated anodizing processes. The system used
205 to create the corrosive environment was a Q-Fog Cyclic Corrosion Chamber
206 (Q-Fog/SSP600, Q-LAB, Florida) in which specimens were exposed to a 5 wt. % NaCl fog
207 for 336 hours, as per ASTM B117 [47]. The acceptance criterion is to form less than five
208 corrosion pits for testing over 336- hour in a salt spray.

209 vii) Electrochemical impedance spectroscopy (EIS) is method widely used to evaluate
210 the corrosion resistance of an anodic coating on aluminum alloys [52-57]. EIS tests were
211 conducted with a precision impedance analyzer Agilent 4294A. An experiment was
212 carried out in a two-electrode arrangement using 1.0 cm^2 test area as the working
213 electrode with the reference electrode Ag/AgCl, $+0.197 \text{ V}$ vs. standard hydrogen
214 electrode. Measurements were conducted in a 3.5 wt. % NaCl solution at room
215 temperature over a frequency range from 40 to 60 MHz with the signal amplitude of 500
216 mV (rms). Tests were conducted on specimens anodized for 30 mins and the presented
217 result is averaged over three repeated anodizing processes.

218 viii) Surface morphology of anodized and untreated specimens was analyzed by
219 scanning electron microscopy (SEM, JEOL JSM-7900F FE-SEM). Energy Dispersive X-
220 Ray Spectroscopy (EDS) scanning of the alloying elements over the surface of anodized
221 and untreated specimens was conducted using the program AZTEC, Oxford
222 Instruments. Two methods of imaging were used to inspect the surface morphology.
223 Secondary electron (SE) imaging, the default setting (LED), was used for inspection of
224 the surface topography. Back-scattered electron (BSE) imaging, BED-C setting, was used
225 to inspect the presence of voids and defects below the specimen surface [58]. All
226 specimens that were anodized, were gold sputtered. Point and ID EDS measurements
227 were analyzed using 10 kV while EDS mapping measurements were analyzed using 20
228 kV using a 45-min acquisition time. Posted in Fig. 3 (a-j), high-magnification SEM
229 images at $100,000\times$ were obtained using 10 kV under LED and the height of the specimen
230 stage, WD, of 10.0 mm. Posted in Fig. 5 (a-t), BSE and SE large scale SEM images at
231 $30,000\times$ were obtained using 10 kV under LED for SE images and BED-C for BSE images,
232 and the height of the specimen stage, WD, of 10 mm. Posted in Fig. 6 (a-e), large- scale
233 SEM images at $30,000\times$ were obtained using 10 kV under LED and the height of the
234 specimen stage, WD, of 10.0 mm. Non-anodized specimen was observed using

27

secondary and backscattered imaging (Fig. 7 (a-b)) and with EDS mapping (Fig. 9(a)). Posted in Fig. 9 (a-k) large scale SEM images at 30,000x were obtained using 20 kV under LED and the height of the specimen stage, WD, of 10.0 mm. A 20 kV beam was used for EDS mapping since mapping with a 10kV beam produced inaccurate data for alloying elements as it utilized $L\alpha$ -peaks for measuring their concentrations. Since the penetration of the 20 kV beam into the specimen was about 2 – 5 μ m, EDS mapping was carried out only on specimens anodized for 30 mins of processing.

The National Institutes of Health (NIH) open-source image processing software ImageJ [59] was used to compute the porosity, pore diameter and the interpore distance in high- magnification SEM images (100,000 \times) (Fig. 3). The processing of an original SEM image combined a sequence of standard ImageJ procedures: Set the image scale in pixels/ μ m based on the scale bar equal to 100 nm; convert image type to 8-bit grayscale; reduce noise and enhance image contrast by using histogram equalization; use flat-field-correction and subtract background to correct for uneven illumination; use a locally adaptive thresholding technique to detect the boundaries between different regions in the image; select a region of interest (ROI) to automatically compute the pore size.

ix) Eq. (5) was used to calculate the efficiency of building an anodic coating, η_{ox} . The anodic efficacy can be described as the ratio of the measured coating mass to the theoretical coating mass computed from the charge transferred during anodization [39]:

$$\eta_{ox} = \frac{m_2 - m_3}{\frac{\eta_{charge} * M_{ox} * Q(t)}{n_{ox} * F}} \quad (5)$$

where m_2 and m_3 are respectively the specimen mass measured after anodization, g/dm², and after removal of the anodic coating, g/dm²; η_{charge} is the charge efficiency; M_{ox} is the molar mass of Al₂O₃ equal to 102 g/mol; Q(t) the cumulative charge transferred per dm²; n_{ox} is the number of electrons associated with the oxide formation [60]; and F is the Faraday's constant (96,500 C/mol). Because η_{charge} is usually close to 1.0 for small anodizing systems, this value was used in calculations.

x) X-ray diffraction (XRD) measurements were conducted on EMPYREAN, Malvern PANalytical, UK at an incident angle 2° in parallel beam geometry with grazing technique, to reduce the signal from the substrate and enhance the signal from the coating, with Rigaku Optima IV diffractometer equipped with CuK α radiation. Two scans at the operating parameters of 40 mA, 45 kV and 0.5° min⁻¹ scanning speed were conducted for every anodized specimen and the presented result is averaged over three repeated anodizing processes. The instrumental broadening of XRD peaks were measured using the National Institute of Standards and Technology Standard (NIST) Reference Material® 1976c consisted of a sintered alumina disc [61].

235

236

237

238

239

240

241

242

243

244

245

246

247

248

249

250

251

252

253

254

255

256

257

258

259

260

261

262

263

264

265

266

267

268

30

xi) The reported percentage difference between two measured values in all tests, val_1 and val_2 was calculated using Eq. (6):

$$\text{Difference (\%)} = 100 \times \frac{|(Val_1 - Val_2)|}{(Val_1 + Val_2)/2} \quad (6)$$

xii) In the statistical analysis of data, measurements of the anodic coating characteristics were arranged in comparison groups: Group 1 (Base, OS1, OS2) and Group 2 (MS1, MS2) as well as in two groups to compare the outcome of processing for 10 mins and 30 mins. The F-test of equality of variances was used to determine whether both populations have the same variance [62]. The null hypothesis of the experiment was a difference between measurements within a particular group compared with the other group appeared by chance. The alternative hypothesis was that this difference was influenced by differences in anodizing processes. The following three-step procedure performed with Analysis of Variance (ANOVA) Microsoft Excel was used for testing the null hypothesis: (1) compute the mean and variance of measurements for each of two groups, (2) compute the overall mean and variance for both groups taken together, and (3) compute the F factor as the ratio between the mean variability of measurements within one group and the mean variability of data within both groups taken together. The value of the F factor will be large only if the variability between the groups is large compared to the variability within both groups taken together. The number of measurements in each group, the total number of measurements and the chosen alpha level, α , that yields the confidence level $100 \cdot (1 - \alpha)\%$ [62]. There are two criteria for rejecting or accepting the null hypothesis. One is to calculate F_α that is a function of α : F should exceed F_α for the null hypothesis to be rejected. The other is to calculate the P_α -value that is a function of α for rejecting, $\alpha > P_\alpha$, or accepting, $\alpha \leq P_\alpha$, the null hypothesis. The reported results of F-tests were conducted for $\alpha = 0.05$ corresponding to the confidence level of 95%.

3. Results and Discussion

3.1 Coating Performance Characteristics

3.1.1 Coating Thickness

33

297
298
299

Anodic coating thickness was measured using an Eddy current meter. Table 3 reports coating thickness measurements (μm) obtained from processes Base, OS1, OS2, MS1, and MS2.

300
301
302
303
304

Table 3. Thickness (μm) of coatings formed in Base, OS1, OS2, MS1, and MS2 processes was measured using an eddy current meter. Anodic samples for testing were taken during 3 stages of the process. The samples were taken at 2-min intervals up to and including 10 mins, and at the end of the process, 30 mins. Statistical analysis of data between processes in Group 1 (Base, OS1, OS2) and Group 2 (MS1, MS2) for the overall process is listed below.

Thickness (μm)							
Process Time, Min	0 to 2	2 to 4	4 to 6	6 to 8	8 to 10	10 to 30	Overall
Base	1.0 \pm 0.3	1.4 \pm 0.4	2.0 \pm 0.4	3.0 \pm 0.5	4.1 \pm 0.4	6.8 \pm 0.5	10.9 \pm 0.7
OS1	0.4 \pm 0.2	0.7 \pm 0.3	1.1 \pm 0.2	1.3 \pm 0.3	1.6 \pm 0.3	7.7 \pm 0.4	9.3 \pm 0.5
OS2	0.8 \pm 0.3	1.2 \pm 0.4	2.0 \pm 0.4	2.2 \pm 0.4	2.7 \pm 0.3	8.0 \pm 0.3	10.7 \pm 0.7
MS1	0.3 \pm 0.1	0.8 \pm 0.3	1.5 \pm 0.4	1.7 \pm 0.4	2.0 \pm 0.3	10.2 \pm 0.4	12.2 \pm 0.4
MS2	0.2 \pm 0.1	1.1 \pm 0.3	1.5 \pm 0.4	2.2 \pm 0.3	2.9 \pm 0.4	9.7 \pm 0.4	12.6 \pm 0.5
Groups	Count	Average	$P_{0.05}$	F	$F_{0.05}$		
Group 1	36	10.3 \pm 0.9	2.70E-14	100.8	4.2		
Group 2	24	12.4 \pm 0.5					

305
306
307
308
309
310
311
312
313
314
315
316
317
318
319
320
321
322

Three time periods were chosen to describe the effect of applying multistep current density vs constant current density on coating build up. The first period, the 10-min ramp, was measured in five, 2-min increments. The current densities used were different for each ramp process and are referenced in Table 2. The final stage of anodization was carried out for 20 mins at the current density stage of 180 A/m² for every process. The rightmost column in Table 3 presents the overall coating thickness.

Multistep processes, MS1 and MS2, formed thicker coatings than coatings produced in the Base process. Noteworthy, the coating thickness formed during the final current density stage for processes, MS1 & MS2, was greater than over the entire OS1 process. The total thickness formed by Base process, 10.9 μm , processes MS1 and MS2 produced 93.6% and 89.0% of that coating thickness in 33% less time. All processes utilizing ramping outperformed the Base process in coating thickness formed during the final 20-min stage of processing. The results of statistical analysis presented in Table 3 demonstrate that a difference between the influence of anodizing processes in Group 1 and Group 2 on the coating thickness is statistically significant as $F > F_{0.05}$ and $0.05 > P_{0.05}$.

36

323

3.1.2 Abrasion Resistance of Anodic Coating

324

325

326

Abrasion resistance was characterized by calculating the weight of the anodic coating removed following 1,000 abrasive cycles. Table 4 lists the weight loss measurements for each specimen.

327

328

329

330

Table 4. Testing results of abrasion resistance, microhardness, acid dissolution and weight loss per micron of specimens anodized in Base, OS1, OS2, MS1, MS2 processes. **Statistical analysis of data between processes in Group 1 (Base, OS1, OS2) and Group 2 (MS1, MS2) for the overall process is listed below.**

Process	Wt. loss (mg) in abrasion tests	Microhardness (MPa)	Wt. loss per coating area (mg/dm ²)	% Loss of total coating	Wt. loss per micron (mg/μm)
Base	39.3 ± 4.1	1282.3 ± 57.6	181.0 ± 11.3	99.6	19.3
OS1	34.8 ± 3.8	1147.4 ± 38.3	169.0 ± 4.9	99.2	21.3
OS2	39.2 ± 4.4	1369.3 ± 20.8	186.0 ± 5.7	99.9	20.2
MS1	26.7 ± 2.0	1398.7 ± 28.1	205.0 ± 8.8	95.2	20.5
MS2	28.7 ± 3.3	1455.1 ± 23.5	227.0 ± 5.2	96.2	21.7

Abrasion					
Groups	Count	Average	P _{0.05}	F	F _{0.05}
Group 1	18	37.8 ± 4.7	4.3E-07	42.8	4.2
Group 2	12	27.7 ± 3.0			

Microhardness					
Groups	Count	Average	P _{0.05}	F	F _{0.05}
Group 1	18	1266.4 ± 103	2.1E-05	26.1	4.2
Group 2	12	1426.9 ± 40			

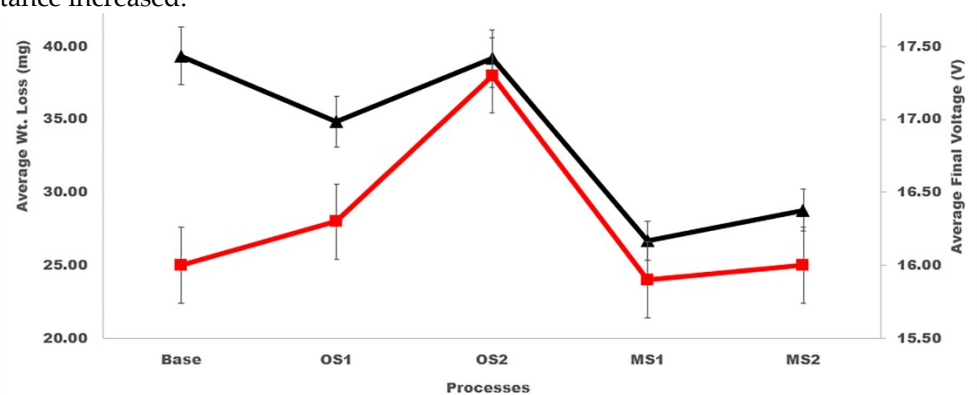
Acid Dissolution					
Groups	Count	Average	P _{0.05}	F	F _{0.05}
Group 1	18	178.7 ± 11.0	6.4E-09	67.2	4.2
Group 2	12	216.0 ± 13.8			

331

39

332
333
334
335
336
337
338

The presented results demonstrate that processes utilizing lower applied voltage, OS1, MS1 and MS2 provided a higher abrasion resistance by 12.1%, 38.2%, and 31.2%, respectively, when compared to the Base process. The results of statistical analysis presented in Table 4 demonstrate that a difference between the abrasion resistance of coatings formed in Group 1 and Group 2 processes is statistically significant as $F > F_{0.05}$ and $0.05 > P_{0.05}$. Plots in Fig. 2 demonstrate as the final voltage decreased, the abrasion resistance increased.



339

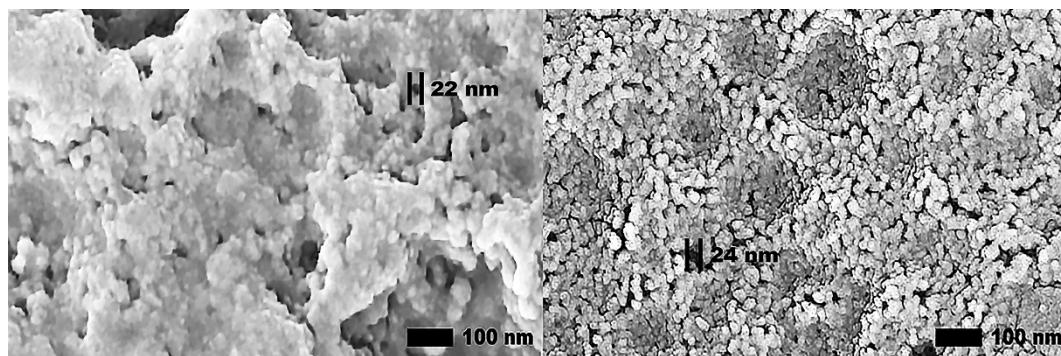
340
341
342

Figure 2. Average wt. loss, mg, versus average final voltage, V. The triangle shape represents the average wt. loss and the square, the average final voltage. A reduction in wt. loss with lower final voltage is noticed in MS1 and MS2.

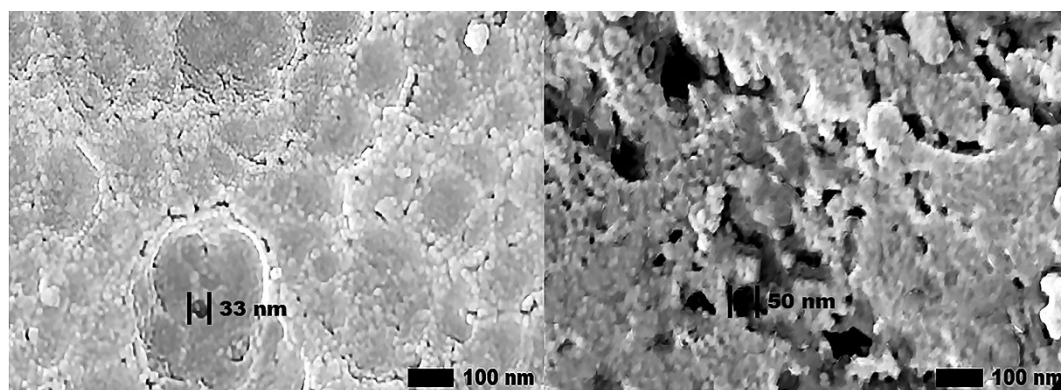
343
344
345
346
347
348
349
350

High-magnification SEM images (100,000x) of anodic coatings posted in Fig. 3 demonstrate a correlation between the increased abrasion resistance and the improvement of the coating morphology. Specifically, these large regions of cracking and pitting formed during anodization are more prominent in the coatings produced by Base and OS2 processes. Coatings subjected to higher voltages, developed areas with surface asperities and porosity. Areas that exhibit these features will become loose upon abrasion.

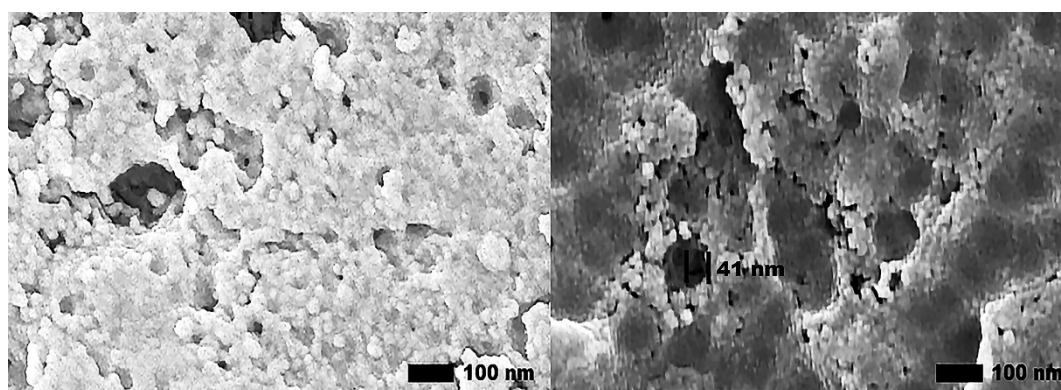
42



351

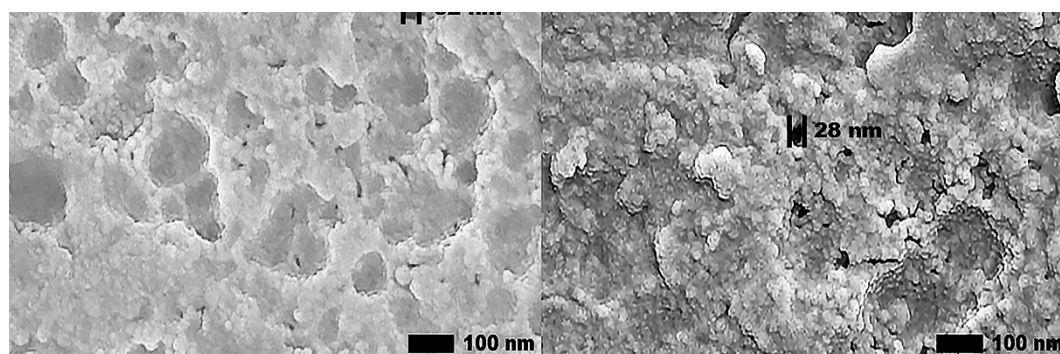


352

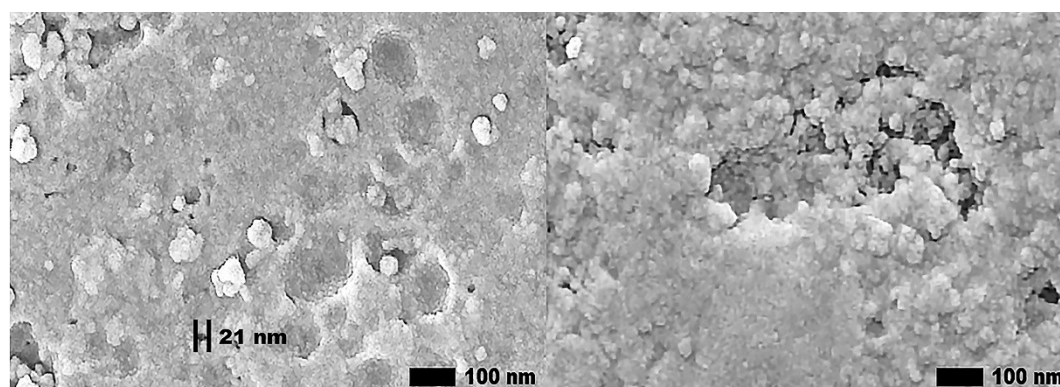


353

45



354



355

356

357

358

359

Figure 3 (a-j). Secondary SEM images (100,000 \times) of the surface morphology reveal circular pores created in the anodization process, respectively, in Base (a-b), OS1 (c-d), OS2 (e-f), MS1 (g-h), and MS2 (i-j) processes. Left images show specimens anodized for 10 mins and right images for 30 mins. Shown pore sizes were computed with ImageJ [59].

360

3.1.3 Microhardness of Anodized Specimens

361

362

363

364

365

366

367

Table 4 lists the average microhardness values in MPa. It is noticeable that the coating hardness increases with the coating thickness, mitigating the softening influence of the aluminum substrate. Compared to standard process Base, hardness of coatings formed in processes OS2, MS1, and MS2 increased by 6.6%, 8.7%, 12.6%, respectively. Process OS1 had an 11.1% reduction in hardness compared to the Base. Hardness measurements presented in Table 4 indicate that the hardness of the material is dependent on the coating thickness. Anodic coatings that were thicker also had higher

48

values of hardness. The results of statistical analysis presented in Table 4 demonstrate that a difference between the influence of anodizing processes in Group 1 and Group 2 on the coating microhardness is statistically significant as $F > F_{0.05}$ and $0.05 > P_{0.05}$.

3.1.4 Anodic Coating Resistance to Acid Dissolution

The resistance to dissolution was characterized by immersing specimens in a chromic and phosphoric acid bath for 15 mins and then calculating the weight of anodic coating removed. Measurements are reported in Table 4 in the following terms: weight loss per coating area, mg/dm^2 , loss of total coating, %, and weight loss per micron, $\text{mg}/\mu\text{m}$. Anodic coatings were completely dissolved on all specimens anodized for 10 mins. Specimens anodized for 30 mins in Base, OS1 and OS2 processes lost more than 99.0% of an anodic coating while specimens anodized in MS1 and MS2 processes lost 95.2% and 96.2%, respectively. Measurements presented in Table 4 demonstrate that anodic coating resistance to acid dissolution increases with coating thickness. As BSE imaging in Fig. 5 illustrate, a reduction of porosity and surface asperities also increased resistance to acid dissolution by reducing the available interstitial regions of a coating to be dissolved. The results of statistical analysis presented in Table 4 demonstrate that a difference between the influence of anodizing processes in Group 1 and Group 2 on the acid dissolution of coatings microhardness is statistically significant as $F > F_{0.05}$ and $0.05 > P_{0.05}$.

3.1.5 Corrosion Resistance of Anodized Specimens

3.1.5.1 Salt Spray (Fog) Testing

Salt Spray (Fog) Testing was conducted on sealed specimens anodized for 10 mins and 30 mins. For specimens anodized for 10 mins, coatings produced by the Base, OS1 and MS2 processes formed 2 ± 1 pits per process. Coatings produced by the OS2 and MS1 processes, formed just one pit per process. For specimens anodized for 30 mins, no pits formed on coatings formed in the Base, OS1, OS2 and MS1 processes, while the MS2 process formed an average of 2 ± 1 pits. The presented results indicate that the coating corrosion resistance is mainly attributed to the ability of sealing the pores and improved with forming a thicker anodic coating.

3.1.5.2 Electrochemical Impedance Spectroscopy (EIS)

368
369
370

371

372

373

374

375

376

377

378

379

380

381

382

383

384

385

386

387

388

389

390

391

392

393

394

395

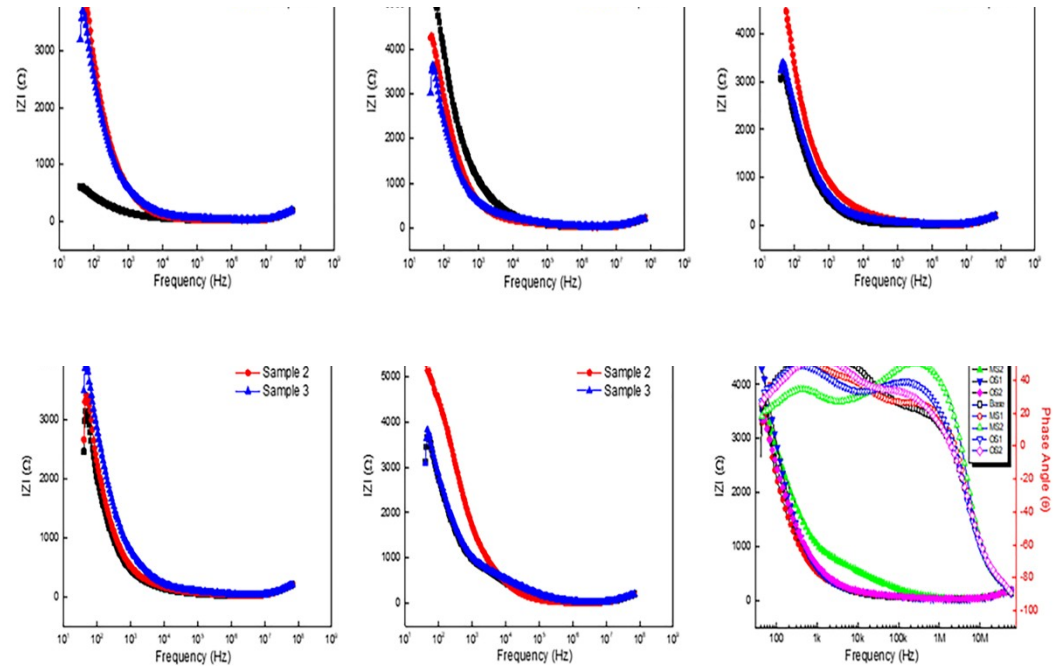
396

397

398

51

399



400

401

402

Figure 4 (a-f). EIS spectra obtained for specimens anodized in processes Base (a), OS1 (b), OS2 (c), MS1 (d), MS2 (e), and Bode Plots (f).

403

404

405

406

407

408

409

410

411

412

413

414

415

416

417

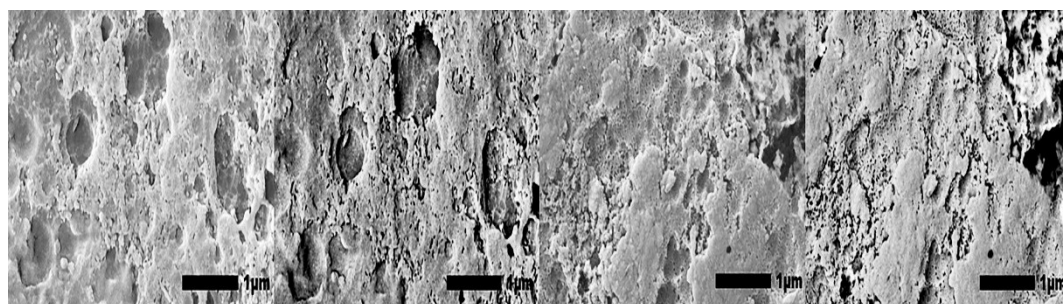
Plots in Fig. 4(a-f) illustrate the EIS response of unsealed specimens anodized for 30 mins. The overall EIS spectra appear to be minimally affected by the anodic coating morphology as all impedance moduli followed a similar cycloid curve with increasing frequency. In the EIS spectrum of anodic specimens, the low frequency region represents properties of the barrier layer and localized corrosion sites, while the high frequency range represents the presence of pores [63]. Plots in Fig. 4(c) and Fig. 4(e) illustrate coatings formed in OS2 and MS2, respectively, exhibit a slightly elevated impedance moduli in the low frequency region below 1kHz. Bode plots in Fig. 4(f) illustrate the EIS spectra of specimens anodized in Base, OS1, OS2, MS1 and MS2 processes. In Fig. 4(f), the impedance moduli decreased with increasing frequency for all processes. The phase angles rapidly depress at high frequencies, with the exception of MS2, that slightly elevates in the region 10 kHz-1 MHz and then reduces similarly to other anodizing processes.

54

3.1.6 SEM/EDS Analysis

Secondary SEM images (100,000x) of anodic coatings posted in Fig. 3 show the surface of coatings anodized in Base, OS1, OS2, MS1 and MS2 processes over 10 and 30 mins. The results demonstrate that multistep ramping of applied current density substantially improved the coating morphology. In all specimens, coatings became more undulated and porous with distinct fragmentation patterns formed during the final stage of anodization. These undesired features are likely caused by increasing nonuniformity in the growth of a coating due to higher voltages used at this stage of the process. Coatings formed in the Base, OS1 and OS2 processes during 10 mins exhibited a porous morphology. This condition was greatly exacerbated at the final period of the 30-min processing. The MS1 and MS2 processes produced coatings that were considerably smoother and less undulated (Fig. 3). The presented results demonstrate that utilizing multistep ramping at the beginning of an anodization process promotes the formation of an anodic coating with a finer morphology and a lower porosity compared to processes without or with a single ramp. Higher potential applied at the beginning of the process inhibits anodic oxidation at certain locations, likely due to the presence of copper and other alloying elements in the coating. Copper contamination can promote uneven film growth and increased electrical resistance.

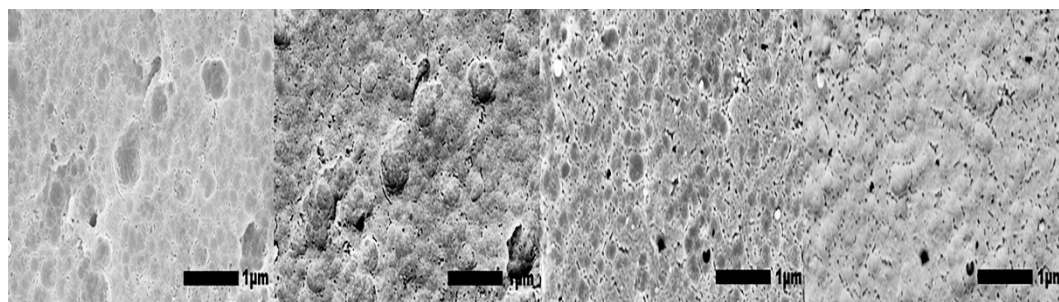
The SE and BSE SEM images posted in Fig. 5 (a-t) provide a large-scale view of the surface of specimens anodized in Base, OS1, OS2, MS1, and MS2 processes for 10 and 30 mins.



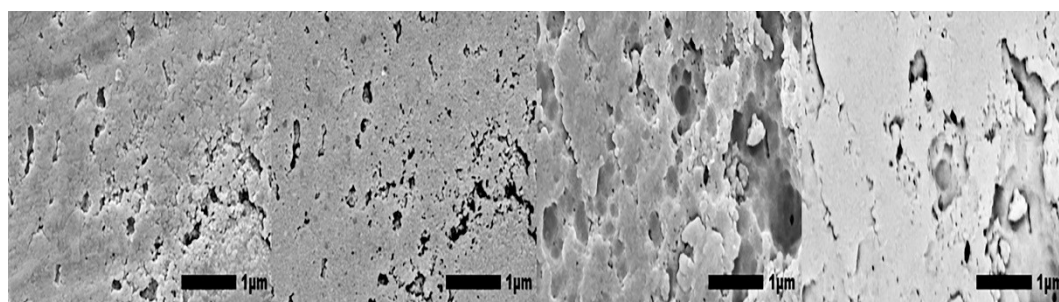
441

442

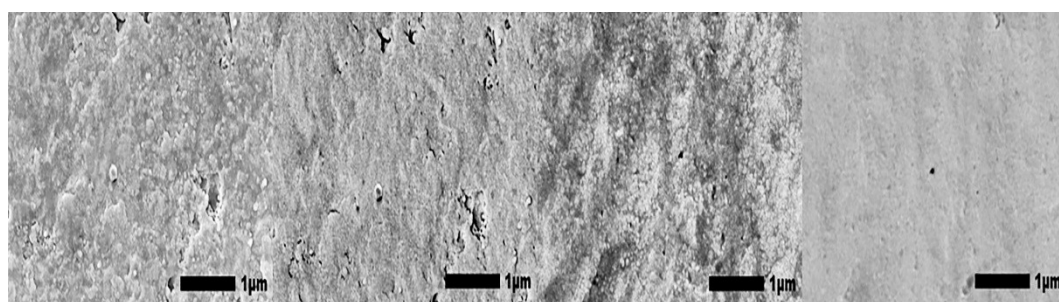
57



443



444



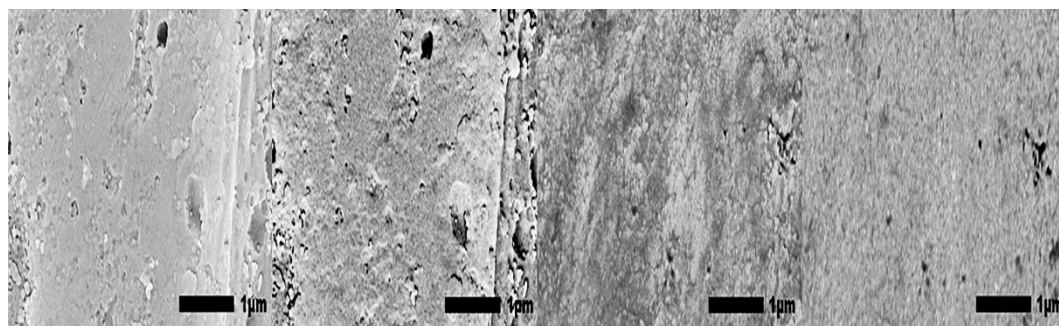
445

446

447

448

60



449

450
451
452
453
454
455
456
457

Figure 5 (a-t). Large-scale SEM images (30,000x magnification) of the coating surface were obtained with the use of back-scattered electrons (BSE) imaging and secondary electrons (SE) imaging: 10 kV under LED for SE images and BED-C for BSE images was used, and the height of the specimen stage, WD, of 10 mm. Specimens anodized respectively in [Base]: a) 10-min SE, b) 10-min BSE, c) 30-min SE, d) 30-min BSE; [OS1]: e) 10-min SE, f) 10-min BSE, g) 30-min SE, h) 30-min BSE; [OS2]: i) 10-min SE, j) 10-min BSE, k) 30-min SE, l) 30-min BSE; [MS1]: m) 10-min SE, n) 10-min BSE, o) 30-min SE, p) 30-min BSE; and [MS2] q) 10-min SE, r) 10-min BSE, s) 30-min SE, t) 30-min BSE.

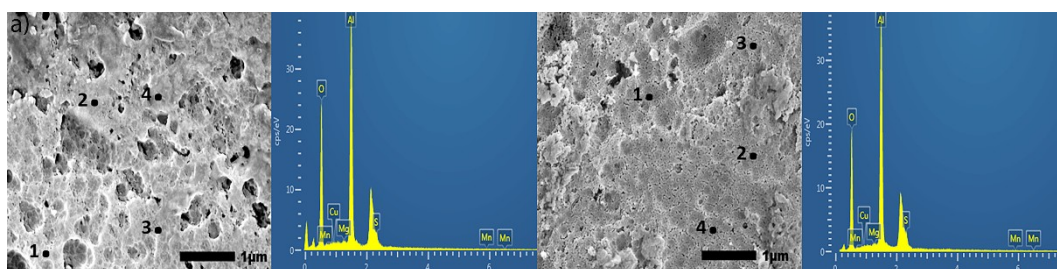
458
459
460
461
462
463
464
465
466
467
468
469
470

The BSE imaging provides a contrasting aspect of the morphology to illustrate the presence of voids, defects, and porosity of the coating, while the SE imaging illustrates the specimen surface topography. Taken together, both types of imaging provide a detailed view of the coating morphology and surface anomalies. In Fig. 5(a-d), the coating produced by the Base process is populated with cracks, voids, and asperities across the entire surface. In Fig. 5(i-l) coatings produced by the OS2 process exhibit similar defects, but to a lesser extent. Coatings formed in the OS1 process (Fig. 5(e-h)) were intact after the ramping period, but eventually became more porous with a longer anodizing time. Processes MS1 and MS2 produced a coating with fewer voids and imperfections as gradual increases in the applied current density allow for formation of more intact, void-free coatings (Fig. 5(m-t)).

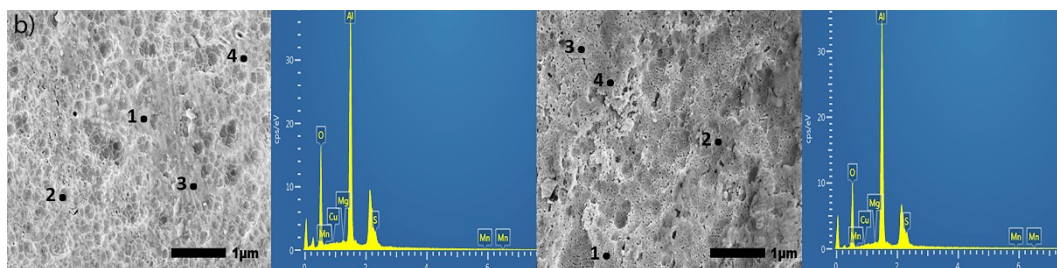
SEM images posted in Fig. 6 provide a large-scale view of the surface of specimens anodized in Base, OS1, OS2, MS1 and MS2 processes for 10 and 30 mins.

63

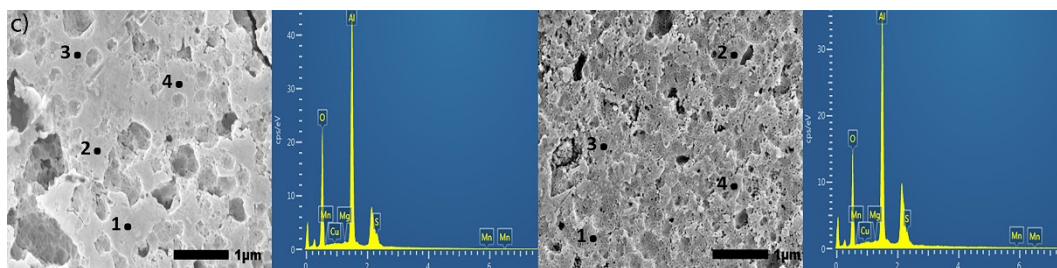
471
472



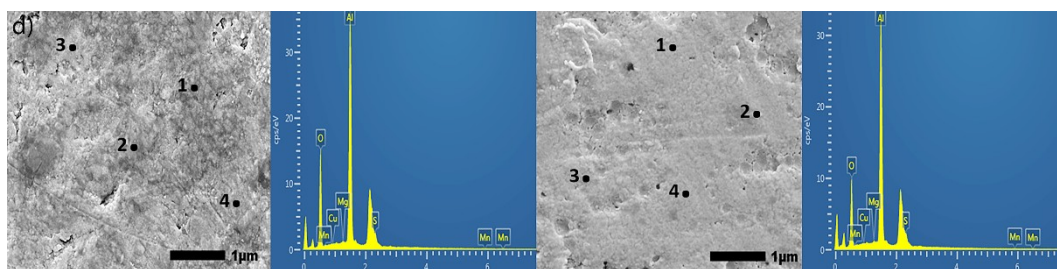
473
474



475
476



477
478



66

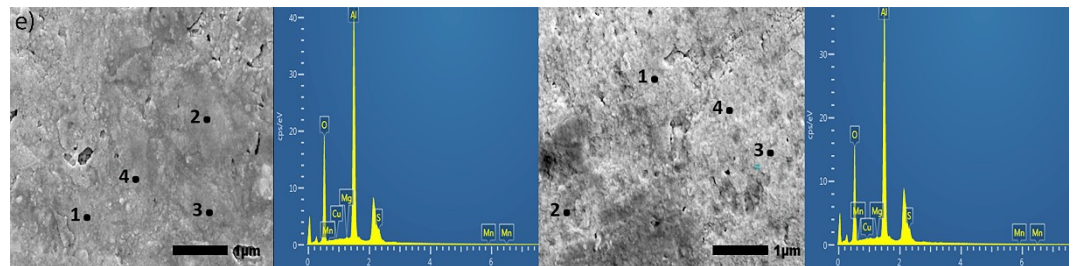


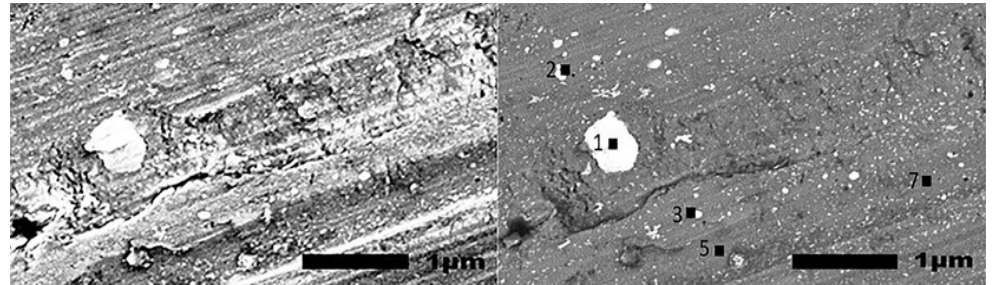
Figure 6 (a-e). Secondary SEM images (30,000x) of specimens anodized in Base (a), OS1 (b), OS2 (c), MS1 (d), and MS2 (e) processes; anodization for 10 mins, left image, and for 30 mins, right image. The EDS analysis was performed at 12 sampling sites in flat, non-pitted regions of the anodic coating. Sites labeled 1 – 4 are representations of the 12 sites chosen. The EDS spectrum shown on the adjacent image is data for site 1.

The Energy Dispersive X-Ray Spectroscopy (EDS) analysis was performed at 12 sampling sites in flat, non-pitted regions. In Fig. 6, sites labeled 1 – 4 are representations of the 12 sites chosen. Two constraints impede the quantification of EDS measurements presented. First, the heights of the peaks for elements Cu, S, Mn, Mg, etc. (Fig. 6) vary from site to site shown in these images due to the inhomogeneity of the coating. Next, the 10 kV beam was used for measurements as the depth of the 20 kV beam penetration was around 2-5 μm . It therefore requires the use of $L\alpha$ characteristic X-ray (keV) for measuring concentrations of these elements that could render the error as high as 3 – 5 wt. % due to peak overlap [64]. For these reasons, reported concentrations of Cu, S, Mg and Mn can be used only as reference points.

The image of an untreated specimen is presented by SE and BSE imaging in Fig. 7(a) and 7(b), respectively. The specimen was chemically cleaned with the same method as the other specimens, to provide detail on the surface prior to anodization. EDS measurements in locations shown in Fig. 7 (b) were taken with particles (1-4) and without (5-8) particles. Presented in Table 1, EDS analysis was conducted to show the composition of these regions. The SE image in Fig. 7(a) and BSE image in Fig. 7(b) demonstrate a difference in local surface compositions, as the lighter color shows particles with a lower content of aluminum and a higher content of O, Cu, Mg, Mn, and Fe compared to the surrounding aluminum rich regions (Table 1).

479
480
481
482
483
484
485
486
487
488
489
490
491
492
493
494
495
496
497
498
499
500
501
502
503

69



504

505

506

507

508

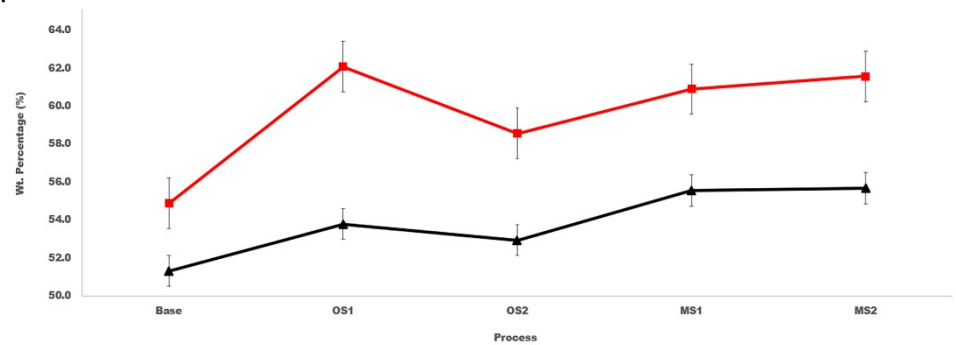
Figure 7 (a-b). SEM images (30,000x) utilizing secondary electron (SE) imaging (a) and back scattered electrons (BSE) (b) of a non-anodized specimen. The EDS analysis was performed at eight locations (4 with particles and 4 without particles) to evaluate the surface composition of a non-anodized specimen.

509

510

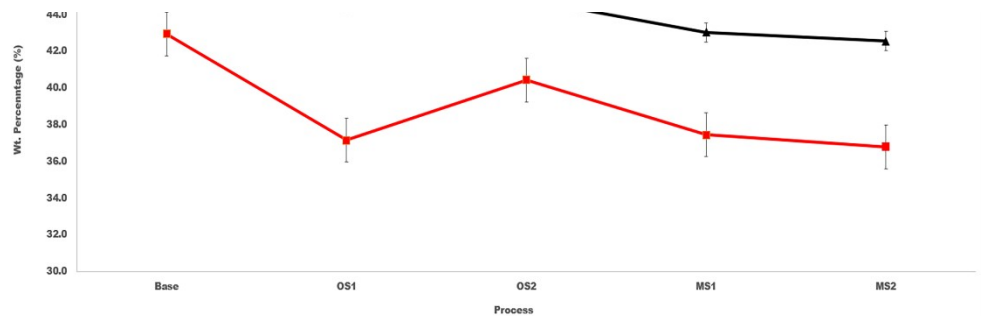
511

Plots in Fig. 8 demonstrate the effect of anodizing processes Base, OS1, OS2, MS1, MS2 on the content of aluminum and oxygen in coatings formed over 10 mins and 30 mins.



512

72



513

514

515

516

Figure 8 (a-b). The amount, wt. %, of (a) aluminum and (b) oxygen at the coating surface of specimens anodized in Base, OS1, OS2, MS1 and MS2 processes over 10 mins and 30 mins. Reported values were averaged over 12 sites depicted in Figure 6.

517

518

519

520

521

522

523

524

525

For all processes, the coatings formed in the 30-min anodizing process had higher wt.% of aluminum and lower wt.% of oxygen when compared to the 10-min process. The atomic Al/O ratios in coatings formed by anodization for 10 mins and 30 mins are listed in Table 5. As can be seen in Fig. 8 (a) and (b) and Table 5, differences between the aluminum and oxygen contents in coatings created by different anodizing processes exceed variations of their concentrations within a coating built under the same anodizing conditions. Compared to Base process, stepwise processes MS1 and MS2 created coatings with the aluminum content larger by 4 - 7 wt.% and the oxygen content lower by 2 - 6 wt.%.

526

527

528

Table 5. The atomic Al/O ratios in coatings formed by anodization over 10 mins and 30 mins in Base, OS1, OS2, MS1 and MS2 processes. Statistical analysis of data for anodization in Group 1 (Base, OS1, OS2) and Group 2 (MS1, MS2) processes over 10 mins and 30 mins is listed below.

Process	Al/O, 10 mins	Al/O, 30 mins
Base	0.69 ± 0.04	0.76 ± 0.05
OS1	0.73 ± 0.05	1.00 ± 0.08
OS2	0.71 ± 0.05	0.86 ± 0.05
MS1	0.77 ± 0.06	0.97 ± 0.06
MS2	0.79 ± 0.06	0.99 ± 0.06

Al/O Ratio – 10 mins					
Groups	Count	Average	P _{0.05}	F	F _{0.05}

75

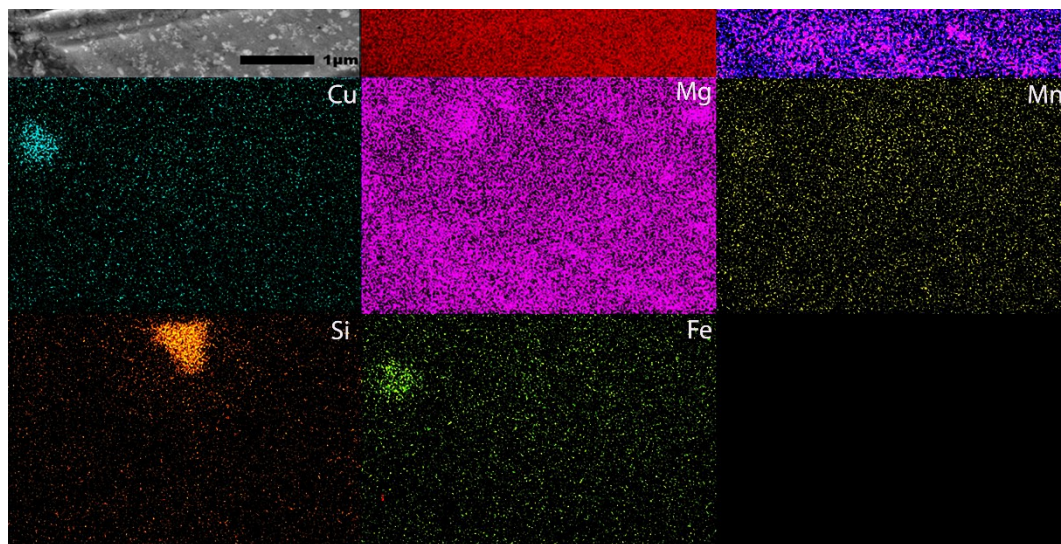
Group 1	36	0.71 ± 0.02	2.3E-05	21.2	4
Group 2	24	0.77 ± 0.06			
Al/O Ratio – 30 mins					
Groups	Count	Average	$P_{0.05}$	F	$F_{0.05}$
Group 1	36	0.87 ± 0.12	0.0002	15.9	4
Group 2	24	0.98 ± 0.06			

The Al/O ratio increases with longer anodizing time and all values are greater than the Al/O stoichiometric ratio of 0.67 in the Al₂O₃ oxide. The results of statistical analysis presented in Table 5 demonstrate that a difference between the Al/O ratio in coatings formed in Group 1 and Group 2 processes is statistically significant as $F > F_{0.05}$ and $0.05 > P_{0.05}$.

SEM images in Figs. 3 and 5, illustrate that utilizing multistep ramping of current density at the beginning of anodization promotes the formation of coating compositions higher in aluminum and lower in oxygen (higher Al/O ratios, Table 5). The EDS maps presented in Fig. 9 were acquired in two EDS runs. They illustrate the distribution of elements over the surface of specimens anodized in processes Base, OS1, OS2, MS1, and MS2 as well as over the surface of an untreated specimen. The EDS mapping image of an untreated specimen (Fig. 9(a)) shows the presence of Fe and Si, mainly in two large particles. The dark particle has a higher concentration of Si and O and is likely a SiO₂ particle, whereas the light particle has a higher concentration of Cu and Fe and is likely an AlCuFe particle [13]. However, Fe and Si were not observed on the surface of anodized specimens. The presence of sulfur seen in images posted in Fig. 9 is likely caused by the absorption of SO₄²⁻ ions penetrating into the anodic coating from the electrolyte. The EDS maps in Fig. 9 clearly demonstrate that concentrations of alloying elements in anodic coatings are very small regardless of slight differences in the distribution of trace elements on the surface of coatings formed by different anodizing processes.

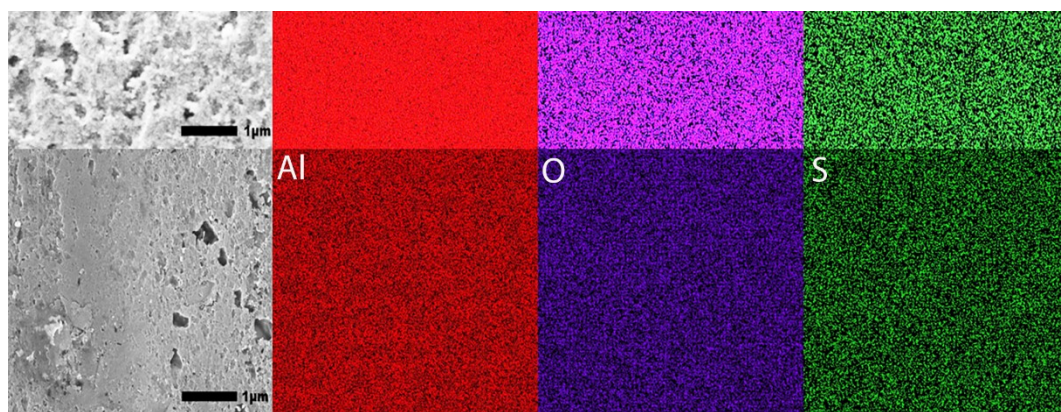
529
530
531
532
533
534
535
536
537
538
539
540
541
542
543
544
545
546
547
548
549
550
551

78



552

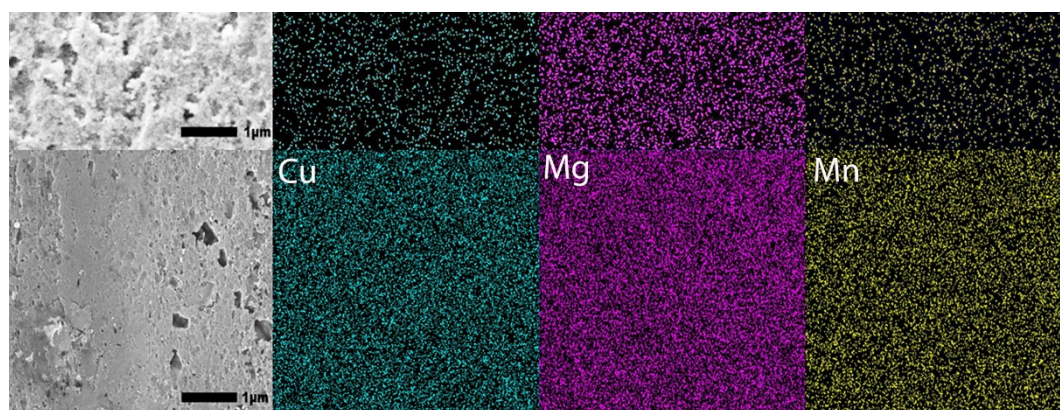
553



554

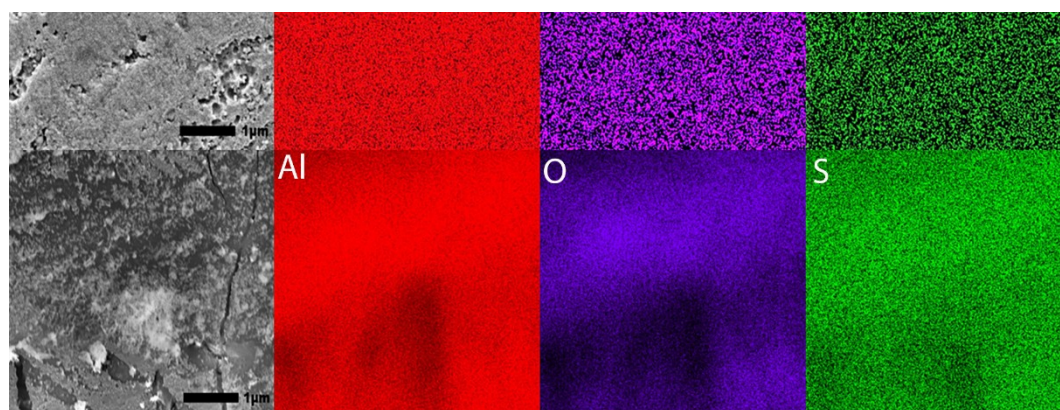
555

81



556

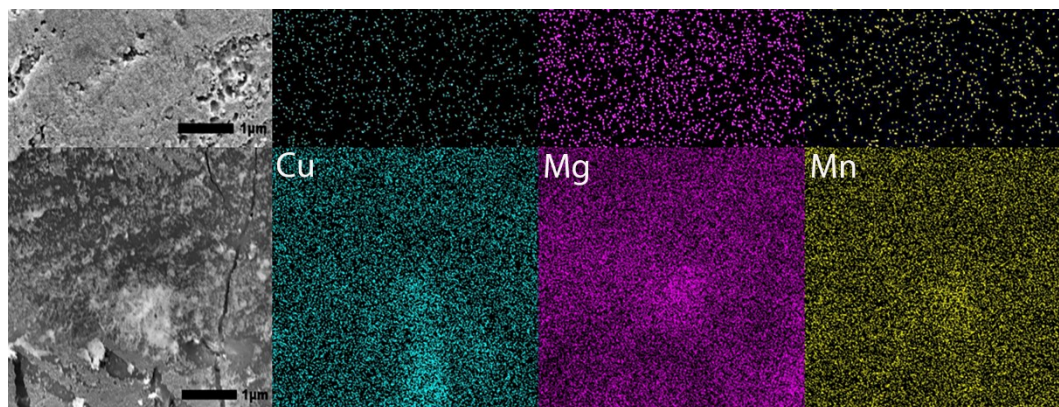
557



558

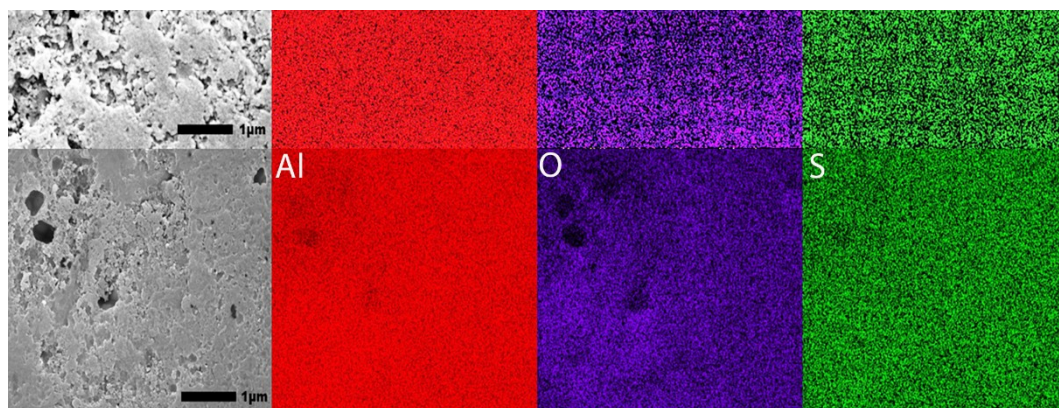
559

84



560

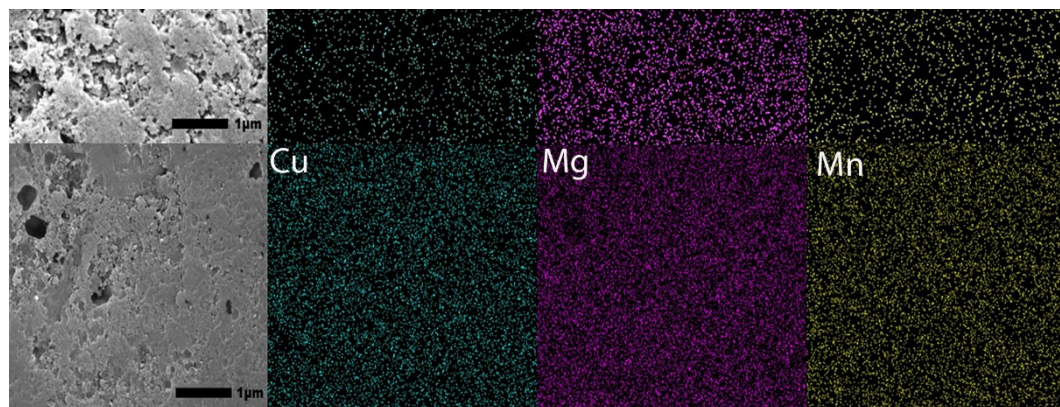
561



562

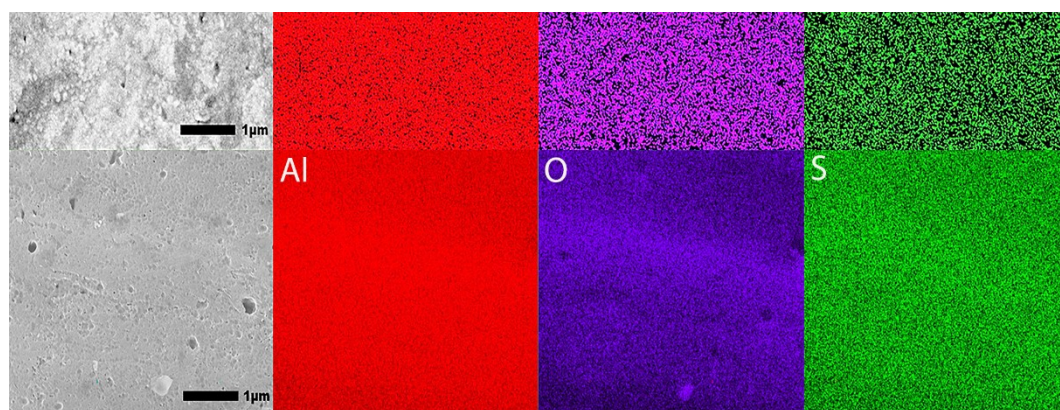
563

87



564

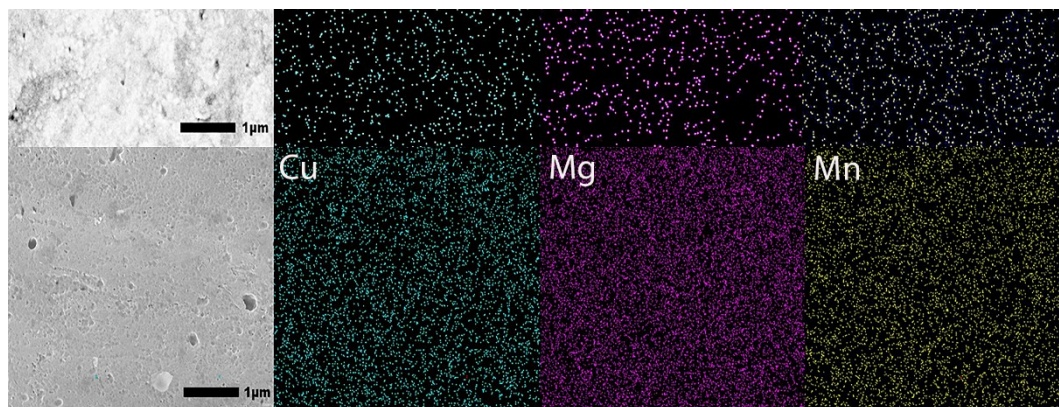
565



566

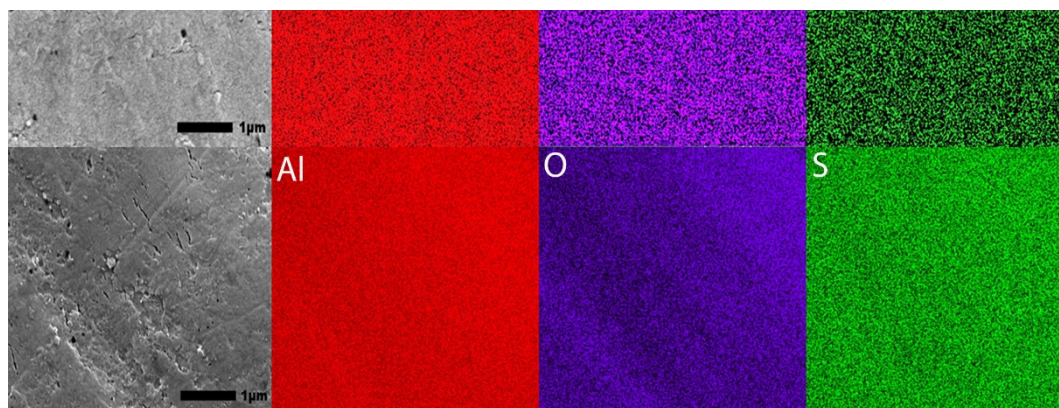
567

90



568

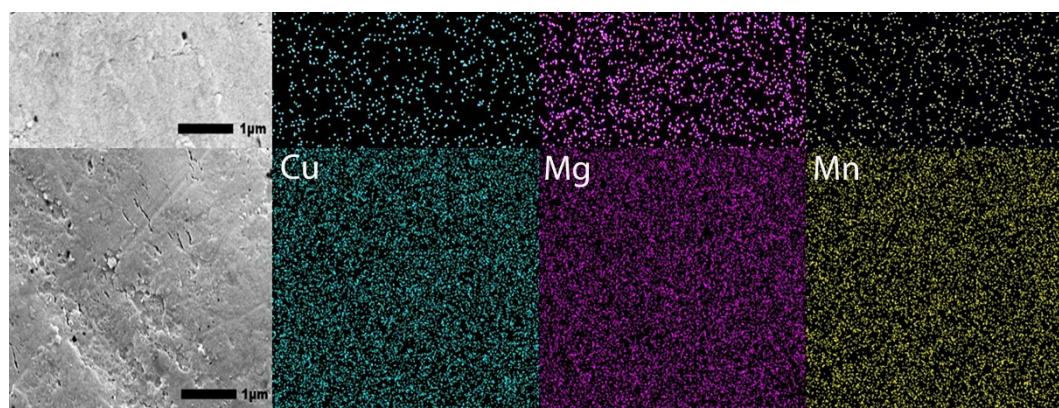
569



570

571

93



572

573

574

575

576

577

578

Figure 9 (a-k). SEM images at 30,000x and EDS mapping images of the surface of (a) an untreated specimen and specimens anodized for 30 mins in processes Base (b-c), OS1 (d-e), OS2 (f-g), MS1 (h-i), and MS2 (j-k). Images were obtained using 20 kV under LED. The acquisition time was about 45 mins to acquire 200 counts/pixel (top row) and 325 counts/pixel (bottom row). Colors representing elements are as follows: Aluminum (red), oxygen (purple), copper (teal), magnesium (pink), manganese (yellow), silicon (orange), iron (lime) and sulfur (green).

579

580

Table 6 lists the values of the pore diameters, interpore distance and pore density computed from SEM images (100,000x) in Fig. 3 with the use of software ImageJ [59].

581

582

583

584

585

586

587

Table 6. Pore diameter (nm), interpore separation (nm) and pore density ($1/\mu\text{m}^2$) in coatings formed by anodization over 10 mins and 30 mins in Base, OS1, OS2, MS1 and MS2 processes. Values were computed from high-magnification SEM images (100,000x) posted in Figure 3 using software ImageJ [59]. Statistical analysis of data between processes in Group 1 (Base, OS1, OS2) and Group 2 (MS1, MS2) for pore diameter (10 & 30 mins), interpore separation and pore density is listed below. Statistical analysis of data between processes in 10 mins and 30 mins for the pore diameter is also listed below.

Process	Pore Diameter, nm		Interpore Separation, nm	Pore Density ($1/\mu\text{m}^2$)
	10 mins	30 mins	30 mins	30 mins
Base	18.3 ± 4.8	33.4 ± 9.2	43.34 ± 0.57	615.2 ± 16.2
OS1	16.5 ± 4.1	26.7 ± 6.7	23.64 ± 0.70	2067.9 ± 120.4
OS2	18.4 ± 6.4	29.3 ± 7.2	39.16 ± 0.34	753.1 ± 12.05
MS1	17.7 ± 5.3	24.9 ± 6.1	22.85 ± 0.85	2214.7 ± 161.6
MS2	17.9 ± 4.8	34.9 ± 5.6	23.05 ± 0.98	2176.6 ± 179.3
Pore Diameter – 10 mins				

96

Groups	Count	Average	P _{0.05}	F	F _{0.05}
Group 1	217	18.2 ± 10.5	0.86	0.03	3.9
Group 2	160	17.7 ± 9.0			

Pore Diameter – 30 mins

Groups	Count	Average	P _{0.05}	F	F _{0.05}
Group 1	192	28.0 ± 9.6	0.01	6.2	3.9
Group 2	120	32.1 ± 8.5			

Pore Diameter – 10 mins vs 30 mins

Groups	Count	Average	P _{0.05}	F	F _{0.05}
10 mins	390	17.9 ± 8.9	3.6E-12	50.1	3.9
30 mins	312	29.6 ± 9.5			

Interpore Distance

Groups	Count	Average	P _{0.05}	F	F _{0.05}
Group 1	9	35.4 ± 9.0	0.005	11.1	4.7
Group 2	6	22.9 ± 1.0			

Pore Density

Groups	Count	Average	P _{0.05}	F	F _{0.05}
Group 1	9	1146 ± 700	0.003	12.8	4.7
Group 2	6	2203 ± 188			

Pore size measurements are illustrated in Figs. 3 (a-j). Pore density was calculated using Eq. (7) [65]:

$$N = \frac{2 \times 10^6}{\sqrt{3} \cdot D_{\text{int}}^2} \quad (7)$$

where N is the number of pores per unit area in μm^2 and D_{int} is the interpore distance in nm. The average pore diameter increase was 49.9%, with the largest increase 64.4% found in the MS2 process. Pores formed at the beginning of anodization have little or no beveling at the pore wall to the adjacent region. The growth of a pore diameter could be

588

589

590

591

592

593

594

99

595 attributed to a higher rate of dissolution around a pore during later stages of processing.
596 The observed dependence of the interpore distance and pore density on the applied
597 initial voltage is consistent with Eq. (8) [66] for the porosity of anodic aluminum oxides
598 formed in sulfuric acid electrolyte:

$$D_{int} = 12.1 + 1.99 \cdot U \quad \text{for} \quad 3 \leq U \leq 18 \quad (8)$$

599 where U is the applied voltage in V. The results of statistical analysis presented in Table
600 6 demonstrate that a difference between data on the diameter of pores formed during 30
601 mins, interpore distance and pore density in coatings formed in Group 1 and Group 2
602 processes is statistically significant as $F > F_{0.05}$ and $0.05 > P_{0.05}$. A difference in
603 measurements of pore diameters in coatings formed in Group 1 and Group 2 processes
604 during 10 mins is not statistically significant. However, a difference between the
605 measurements of pore diameters in all coatings formed during 10 mins and 30 mins of
606 anodization is statistically significant as $F > F_{0.05}$ and $0.05 > P_{0.05}$.

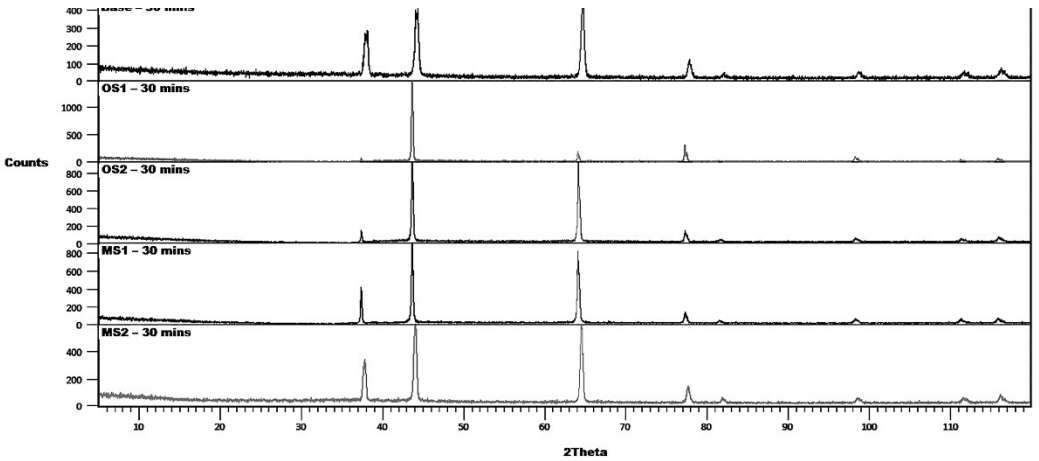
607 3.1.7 XRD Patterns of Anodized Specimens

608 XRD of anodic coatings formed in Base, OS1, OS2, MS1 and MS2 processes over 10
609 mins and 30 mins are shown in Fig. 10. Measurements were conducted at an incident
610 angle of 2° using a grazing technique. For comparison, XRD of untreated specimens are
611 also shown in Fig. 10. According to the instrument peak profiles, eight peaks in XRD
612 patterns corresponded to the aluminum face-centered-cubic (fcc) crystal structure.
613 However, shifts and changes in the intensity of diffraction peaks of aluminum oxides
614 were observed in diffraction patterns collected on specimens anodized for 10 mins (Fig.
615 10(a)) and 30 mins (Fig. 10(b)). It indicates that amorphous aluminum oxides formed in
616 the anodizing process.
617

102



618



619

620

621

622

Figure 10 (a-b). XRD of the untreated specimen alloy and specimens anodized in Base, OS1, OS2, MS1, MS2 process (a) for 10 mins and (b) for 30 mins. Measurements collected at an incident angle of 2° using a grazing technique.

623

624

625

626

Compared to the untreated specimen, anodization changed the position, width, and intensities of peaks in diffraction patterns. Lattice constants of the fcc structure of anodized specimens are reported in Fig. 11 (a) and was computed for both types of XRD measurements from Eq. 9 [67]:

105

$$d_{hkl} = \frac{a}{\sqrt{h^2 + k^2 + l^2}} \quad (9)$$

627

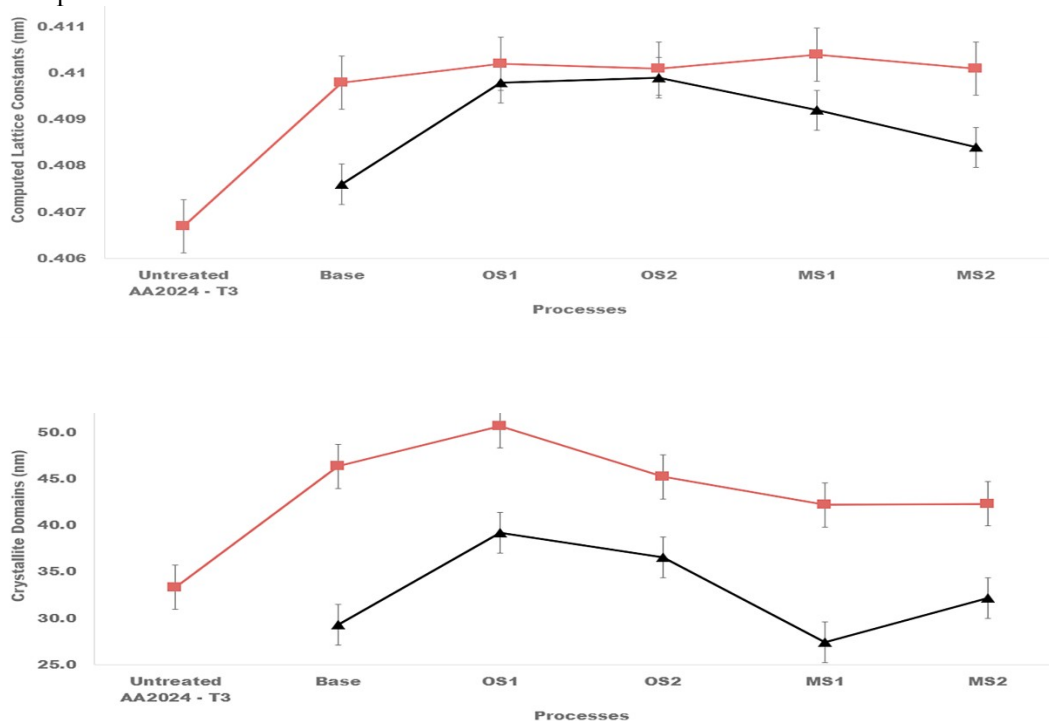
628

629

630

631

where d_{hkl} is the distance between the adjacent lattice planes in the fcc structure for the peak Bragg angle in nm, a is the lattice constant/parameter in nm, and hkl are the Miller indices for the lattice planes. Results of these calculations presented in Fig. 11(a) were averaged over all fcc peaks in the diffraction pattern and then averaged over three specimens.



632

633

634

635

636

637

Figure 11 (a-b). Computed (a) lattice constants of the fcc structure of crystallites and (b) sizes of crystalline domains for specimens anodized in Base, OS1, OS2, MS1, MS2 process for 10 mins and for 30 mins. Reported values were averaged over all peaks identified in the diffraction pattern and then averaged over three specimens.

638

639

Plots in Fig. 11(a) show that anodization increased the lattice constants of crystallites and that they are larger for the entire process. The Scherrer equation, Eq. (10)

108

640
641

[67], was taken to compute the size of coherently scattering crystalline domains from the peak width:

$$L = \frac{K\lambda}{\beta_{hkl} \cos(\theta_{hkl})} \quad (10)$$

642
643
644
645
646
647

where L is the mean size of the crystalline domains in nm, $K=0.9$ is the shape factor, $\lambda=0.15406$ nm is the wavelength of the $\text{CuK}\alpha$ radiation, θ_{hkl} is the peak Bragg angle in radians, β_{hkl} is the corrected value of the width at half-maximum (FWHM) of the peak in radians, and hkl are the Miller indices of the crystallographic planes. The measured broadening, Eq. (11) [67], of a peak was corrected by the data on the instrumental peak broadening as:

$$\beta_{hkl} = (\beta_{m,hkl}^2 - \beta_{ints,hkl}^2)^{1/2} \quad (11)$$

648
649
650
651
652
653
654

where $\beta_{m,hkl}$ (rad) is the measured FWHM, and $\beta_{inst,hkl}$ (rad) is the instrumental FWHM measured using the NIST standard [46]. Results of these calculations shown in Fig. 11(b) were averaged over all peaks identified in the diffraction pattern and then averaged over three specimens. As can be seen from Fig. 11(b), anodization increased the size of crystalline domains and that they were increasing with the processing time.

3.2 Process Efficiency

655
656
657
658
659
660

Table 7 reports the values of an applied voltage needed to maintain the designed current density in processes Base, OS1, OS2, MS1 and MS2. Differences between the charge transferred per step and the overall charge transferred listed in Table 2 and Table 7 are lying within several percentages as the accuracy of maintaining the constant anodizing current was about 1%. The values of the applied voltage needed to initiate anodization was lower in processes OS1, MS1 and MS2 (Table 7).

661
662
663

Table 7. Data on the applied anodizing current, initial and final voltage, and measurements of charge for each step of Base, OS1, OS2, MS1 and MS2 processes. The presented values were averaged over three runs.

Process	Mins	Amperage, A	Charge, C	Initial Voltage, V	Final Voltage, V
Base	30	17	29800.0	15.7 ± 0.5	16.0 ± 0.2
			\pm		
OS1	10	3	2332.2	5.8 ± 0.2	9.0 ± 0.3
			1710.0 ± 98.1		

111

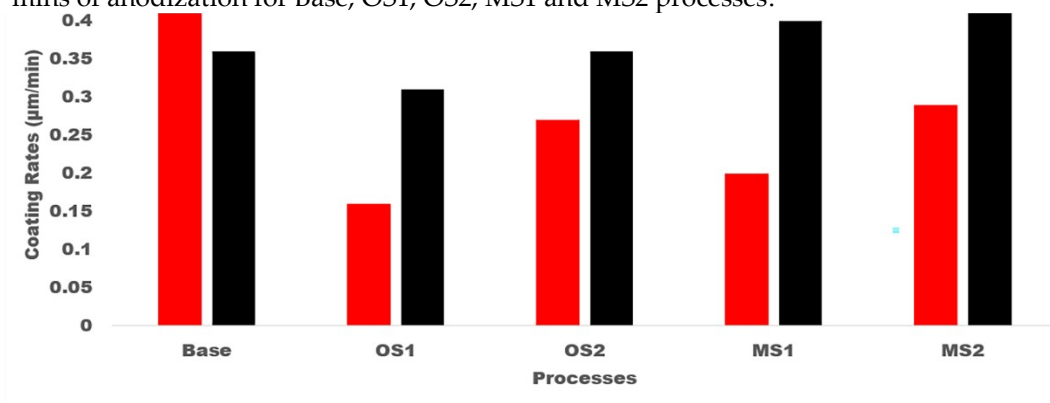
	20	17	19755.0 ± 347.6	15.8 ± 0.2	16.3 ± 0.6
OS2	10	11	6005.0 ± 97.9	13.6 ± 0.4	14.6 ± 0.1
	20	17	18852.0 ± 282.4	15.5 ± 0.2	17.3 ± 0.2
MS1	2	3	333.0 ± 27.3	5.4 ± 0.2	7.4 ± 0.5
	2	4	444.0 ± 25.7	8.6 ± 0.2	8.9 ± 0.6
	2	5	563.0 ± 16.2	9.2 ± 0.2	9.5 ± 0.3
	2	5	598.0 ± 36.8	9.8 ± 0.1	10.2 ± 0.1
	2	6	716.0 ± 94.2	10.5 ± 0.2	10.8 ± 0.1
	20	17	20165.0 ± 266.9	14.1 ± 0.1	15.9 ± 0.1
MS2	2	3	339.0 ± 16.8	5.5 ± 0.5	7.5 ± 0.7
	2	6	705.0 ± 22.9	9.3 ± 0.5	10 ± 0.6
	2	9	998.0 ± 63.5	11.2 ± 0.4	11.5 ± 0.4
	2	12	1410.0 ± 84.2	13.0 ± 0.7	13.2 ± 0.6
	2	15	1715.0 ± 114.2	13.5 ± 0.7	14.1 ± 0.7
	20	17	19965.0 ± 201.3	14.4 ± 0.4	16.0 ± 0.4

664

665

666

Fig. 12 illustrates the coating growth rates, $\mu\text{m}/\text{min}$, computed for 10 mins and 30 mins of anodization for Base, OS1, OS2, MS1 and MS2 processes.



667

668

669

670

Figure 12. Coating growth rates, $\mu\text{m}/\text{min}$, in processes Base, OS1, OS2, MS1, and MS2. Anodizing times were 10 mins and 30 mins. Overall growth rates are shown on the right. Multistep processes, MS1 and MS2, provide the highest overall growth rates.

671

672

The presented results demonstrate that utilizing multistep ramping of current density at the beginning of anodization allow for a higher growth rate over the 10-30

117

683

684

685

686

687

688

689

690

691

692

693

694

695

696

697

698

699

700

701

702

703

704

705

706

707

708

709

710

711

712

713

714

715

716

717

718

719

720

721

Results presented in Table 8 show that all stepwise processes reduced the overall values of the charge transferred per unit thickness. In particular, it was reduced by 37.5% and 31.3%, respectively, for multistep processes MS1 and MS2. The results of statistical analysis presented in Table 8 demonstrate that a difference between data on the thickness of coatings formed in Group 1 and Group 2 processes is statistically significant as $F > F_{0.05}$ and $0.05 > P_{0.05}$.

Table 7 presents the measurements of voltage used to compute the work required to transfer an electric charge during anodization. Table 9 summarizes these calculations for Base, OS1, OS2, MS1 and MS2 processes.

Table 9. Coating efficiency, η_{ox} , of anodization, average voltage, V, and work, kJ, calculated for Base, OS1, OS2, MS1, and MS2 processes. Statistical analysis of data between processes in Group 1 (Base, OS1, OS2) and Group 2 (MS1, MS2) for the overall process is listed below.

Process	Coating Efficiency, (η_{ox})	Average Voltage, V	Work (kJ)		
Base	0.201 ± 0.006	15.9 ± 0.2	14334 ± 152		
OS1	0.233 ± 0.005	13.2 ± 0.2	10475 ± 219		
OS2	0.211 ± 0.001	15.6 ± 0.1	12926 ± 127		
MS1	0.245 ± 0.011	13.0 ± 0.1	10862 ± 85		
MS2	0.267 ± 0.003	13.7 ± 0.4	12039 ± 299		
Efficiency					
Groups	Count	Average	$P_{0.05}$	F	$F_{0.05}$
Group 1	9	0.215 ± 0.015	1.7E-05	26.8	4.7
Group 2	6	0.256 ± 0.015			
Average Voltage					
Groups	Count	Average	$P_{0.05}$	F	$F_{0.05}$
Group 1	9	14.9 ± 1.3	0.02	6.5	4.7
Group 2	6	13.3 ± 0.7			
Work					
Groups	Count	Average	$P_{0.05}$	F	$F_{0.05}$
Group 1	9	12578 ± 1700	0.15	2.3	4.7
Group 2	6	11450 ± 796			

Table 9 presents data on anodic process efficiency, η_{ox} , that was computed from Eq. 5. Results reported in Table 9 demonstrate that stepwise processes reduce the work and applied voltage needed to build an anodic coating and thereby raise the anodization efficiency. Compared to Base, processes MS1 and MS2 are more efficient by 19.7% and 28.2%, respectively. The results of statistical analysis presented in Table 9 demonstrate that a difference between data on the

120

722

723

724

725

726

727

728

729

730

731

732

733

734

735

736

737

738

739

740

741

742

743

744

745

746

747

748

749

750

751

752

753

754

755

756

757

758

efficiency and average voltage of anodizing processes in Group 1 and Group 2 is statistically significant as $F > F_{0.05}$ and $0.05 > P_{0.05}$. However, a difference in data on the work between processes in Groups 1 and 2 is not statistically significant.

4.0 Conclusions

The presented results demonstrated the advantages of current density ramping on the growth rate, structure, and service properties of AA2024 – T3 alloy. Five anodizing processes in a sulfuric acid bath were studied: a conventional Base process with a constant applied current density and ramping processes, OS1, OS2, MS1, MS2, applying different magnitudes of current density in either one or five steps. Increasing the number of ramping stages with an incremental rise in current density in processes MS1 and MS2 lowered the oxygen infusion into the coating (Al/O ratio), raised the coating growth rate, reduced the coating porosity, and enhanced the coating abrasion resistance and hardness. Overall, processes MS1 and MS2 were 11.3% and 14.5% faster at producing 1 μm of coating per minute compared to the Base process and formed almost the same thickness in 33% less time. Both multistep ramp processes, MS1 and MS2, produced a thicker coating compared to single-step ramp processes. Multistep processes MS1 and MS2 were, respectively, 19.7% and 28.2% more efficient in building an anodic coating compared to the Base process.

In our previous work [15] we demonstrated that it was possible to improve the properties of anodized 7075 – T6 aluminum alloy by gradually increasing the current density during the ramp stage. That result taken together with the presented data on anodization of AA2024 – T3 show that benefits of multistep anodization processes are not sensitive to the alloy composition. We expect that the use of multistep anodization with a gradual increase in an applied current density would allow for the development of more efficient anodization processes for other aluminum alloys.

Author Contributions:

Peter Totaro: Conceptualization, Methodology, Experiments, Data curation and analysis, Writing—original draft, review & editing.

Boris Khusid: Supervision, Conceptualization, Data curation and analysis, Writing – review & editing

Funding: This research did not receive any specific grant from funding agencies in the public, commercial, or not-for-profit sectors.

Acknowledgments: The authors are thankful to Dr. Xueyan Zhang and Dr. Jeong Seop Shim (Material Characterization Laboratory, New Jersey Institute of Technology, New Jersey) for help in conducting SEM imaging, EDS analysis, XRD analysis and interpretation of data. The authors

123

759 are thankful to Dr. Sagnik Basuray and Zhenglong Li (New Jersey Institute of Technology, New
760 Jersey) for help in conducting EIS measurements and interpretation of data.

761 **Conflicts of Interest:** The authors declare no conflict of interest.

762 References

- 763 [1] Sheasby, P.G.; Pinner, R. *The Surface Treatment and Finishing of Aluminum*
764 *and Its Alloys*, 6th ed., Finishing Publications Ltd. and ASM International, Materials
765 Park, Ohio, 2001.
- 766 [2] Ostovan, F., Amanollah, S., Toozandehjani, M., & Shafiei, E. Fabrication of
767 Al5083 surface hybrid nanocomposite reinforced by CNTs and Al₂O₃ nanoparticles
768 using friction stir processing. *J. Compos. Mater.* **2020** *54* 1107–1117.
769 <https://doi.org/10.1177/0021998319874849>
- 770 [3] Ostovan, F., Azimifar, I., Toozandehjani, M., Shafiei, E., Shamshirsaz, M.
771 Synthesis of ex-situ Al5083 reinforced with mechanically-alloyed CNTs and Fe₂O₃
772 nanoparticles using friction stir processing. *J. Appl. Res. Technol.* **2021** *14* 1670–1681.
773 <https://doi.org/10.1016/j.jmrt.2021.07.072>
- 774 [4] Serdechnova M, Karpushenkov SA, Karpushenkava LS, et al. The influence of
775 PSA pre-anodization of AA2024 on PEO coating formation: composition,
776 microstructure, corrosion, and wear behaviors. *Materials* **2018** *11* 2428.
777 [doi:10.3390/ma11122428](https://doi.org/10.3390/ma11122428)
- 778 [5] Lu, J.; Wei, G.; Yu, Y.; Guo, C.; Jiang, L. Aluminum alloy AA2024 anodized
779 from the mixed acid system with enhanced mechanical properties. *Surf. Interface* **2018**
780 *13* 46–50. <https://doi.org/10.1016/j.surfin.2018.08.003>
- 781 [6] Jani, A.; Losic, D.; Voelcker, N.H. Nanoporous anodic aluminum oxide: ad-
782 vances in surface engineering and emerging application. *Prog. Mater. Sci.* **2018** *58* 636–
783 704. <https://doi.org/10.1016/j.pmatsci.2013.01.002>
- 784 [7] Zhao, X.; Wei, G.; Meng, X.; Zhang, A. High performance alumina films pre-
785 pared by direct current plus pulse anodisation. *Surf. Eng.* **2014** *30* 455–459. <https://doi.org/10.1179/1743294414Y.0000000258>
- 786 [8] Meng, X.F.; Wei, G.; Zhao, X.; Ge, H. Study on anodic oxidation of 2024 alu-
787 minum alloys in sulfuric-citric acid. *Mater. Sci. Forum* **2014** *788* 236–242. <https://doi.org/10.4028/www.scientific.net/MSF.788.236>
- 788 [9] Shabestari, S.G.; Ghoncheh, M.; Momeni, H. Evaluation of formation of inter-
789 metallic compounds in Al2024 alloy using thermal analysis technique. *Thermochim.*
790 *Acta* **2014** *589* 174–182. <https://doi.org/10.1016/j.tca.2014.05.024>

126

- 793 [10] Chen, Y.; Gao, N.; Sha, G.; Ringer, S. P.; Starink, M. J. Microstructural evolution,
794 strengthening and thermal stability of an ultrafine-grained Al–Cu–Mg alloy. *Acta*
795 *Mater* **2016** 109 202–212. <https://doi.org/10.1016/j.actamat.2016.02.050>
- 796 [11] Zhang, F.; Levine, L.E.; Allen, A.J.; Campbell, C. E.; Creuziger, A. A.; Kazant-
797 seva, N.; Ilavsky, J. In situ structural characterization of ageing kinetics in aluminum
798 alloy 2024 across angstrom-to-micrometer length scales. *Acta Mater.* **2016** 111 385–398.
799 <https://doi.org/10.1016/j.actamat.2016.03.058>
- 800 [12] Wang, S.; Starink, M. J. Precipitates and intermetallic phases in precipitation
801 hardening Al–Cu–Mg–(Li) based alloys. *Int. Mater. Rev* **2005** 50 193–215. <https://doi.org/10.1179/174328005X14357>
- 802 [13] Bononi, M.; Giovanardi, R.; Bozza, A.; Mattioli, P. Pulsed current effect on hard
803 anodizing process of 2024-T3 aluminium alloy. *Surf. Coat. Technol* **2016** 289 110–117.
804 <https://doi.org/10.1016/j.surfcoat.2016.01.056>
- 805 [14] Kaufman, J.G. Corrosion of Aluminum and Aluminum Alloys, ASM Interna-
806 tional, Materials Park, Ohio, 2005.
- 807 [15] Totaro, P.; Khusid, B. Multistep anodization of 7075 – T6 aluminum alloy. *Surf.*
808 *Coat. Technol* **2021** 421 127407. <https://doi.org/10.1016/j.surfcoat.2021.127407>
- 809 [16] Runge, J.M. The Metallurgy of Anodizing Aluminum: Connecting Science to
810 Practice, Springer International Publishing AG, 2018.
- 811 [17] Cooke, W.E. Factors affecting loss of brightness and image clarity during an-
812 odizing of bright trim aluminum alloys in sulfuric acid electrolyte. *Plating* **1962** 49
813 1157–1165.
- 814 [18] Chung C.K.; Chang, W.; Liao, M.; Chang, H. Effect of pulse voltage and alu-
815 minium purity on the characteristics of anodic aluminum oxide using hybrid pulse
816 anodization at room temperature. *Thin Solid Films* **2011** 519 15 4754–4758. <https://doi.org/10.1016/j.tsf.2011.01.029>
- 817 [19] Roshani, M.; Sabour Rouhaghdam, A.; Aliofkhazraei, M.; Heydari Astaraee, A.
818 Optimization of mechanical properties for pulsed anodizing of aluminum. *Surf. Coat.*
819 *Technol* **2017** 310 17–24. <https://doi.org/10.1016/j.surfcoat.2016.12.046>
- 820 [20] Iglesias-Rubianes, L.; Garcia-Vergara, S.; Skeldon, P.; Thompson, G.; Ferguson,
821 J.; Beneke, M. Cyclic oxidation process during anodizing of Al–Cu alloys. *Electrochim.*
822 *Acta* **2007** 52 7148–7157. <https://doi.org/10.1016/j.electacta.2007.05.052>
- 823
824

129

- 825 [21] Zhou, X.; Thompson, G.; Habazaki, H.; Shimizu, K.; Skeldon, P.; Wood, G. Cop-
826 per enrichment in Al–Cu alloys due to electropolishing and anodic oxidation. *Thin*
827 *Solid Films* **1997** 293 327–332. [https://doi.org/10.1016/S0040-6090\(96\)09117-1](https://doi.org/10.1016/S0040-6090(96)09117-1)
- 828 [22] Saenz de Miera, M.; Curioni, M.; Skeldon, P.; Thompson, G. E. Preferential an-
829 odic oxidation of second-phase constituents during anodizing of AA2024-T3 and
830 AA7075-T6 alloys. *Surf. Interface Anal* **2010** 42 241–246. <https://doi.org/10.1002/sia.3191>
- 831 [23] Pakes, A.; Thompson, G.; Skeldon, P.; Morgan, P. Development of porous an-
832 odic films on 2014-T4 aluminium alloy in tetraborate electrolyte. *Corros. Sci* **2003** 45
833 1275–1287. [https://doi.org/10.1016/S0010-938X\(02\)00216-0](https://doi.org/10.1016/S0010-938X(02)00216-0)
- 834 [24] Vignoli, M., Dick, A., Knörnschild, P., Dick, L.F. The effect of different car-
835 boxylic acids on the sulfuric acid anodizing of AA2024. *Surf. Coat. Technol* **2020** 383
836 125283–. <https://doi.org/10.1016/j.surfcoat.2019.125283>
- 837 [25] Elaish, R., Curioni, M., Gowers, K., Kasuga, A., Habazaki, H., Hashimoto, T.,
838 Skeldon, P. Effect of fluorozirconic acid on anodizing of aluminium and AA 2024-T3
839 alloy in sulphuric and tartaric-sulphuric acids. *Surf. Coat. Technol* **2018** 342 233–243.
840 <https://doi.org/10.1016/j.surfcoat.2018.02.096>.
- 841 [26] Schneider, M., Liebmann, T., Langklotz, U., & Michaelis, A. Microelectrochemi-
842 cal investigation of anodic oxide formation on the aluminum alloy AA2024. *Elec-*
843 *trochim. Acta* **2017** 249 198–205.
844 <https://doi.org/10.1016/j.electacta.2017.07.160>
- 845 [27] Ma, S.; Luo, P.; Zhou, H.; Fu, C.; Kuang, Y. Preparation of anodic films on 2024
846 aluminum alloy in boric acid-containing mixed electrolyte. *Trans. Nonferrous Met*
847 **2008** 18 825–830. [https://doi.org/10.1016/S1003-6326\(08\)60143-0](https://doi.org/10.1016/S1003-6326(08)60143-0)
- 848 [28] Li, Y.; Zhang, Y.; Li, S.; Zhao, P. Influence of adipic acid on anodic film forma-
849 tion and corrosion resistance of 2024 aluminum alloy. *Trans. Nonferrous Met* **2016** 26
850 492–500. [https://doi.org/10.1016/S1003-6326\(16\)64137-7](https://doi.org/10.1016/S1003-6326(16)64137-7)
- 851 [29] Elabar, D., La Monica, G., Santamaria, M., Di Quarto, F., Skeldon, P., Thomp-
852 son, G. Anodizing of aluminium and AA 2024-T3 alloy in chromic acid: Effects of sul-
853 phate on film growth. *Surf. Coat. Technol* **2017** 309 480–489. <https://doi.org/10.1016/j-surfcoat.2016.11.108>
- 854
- 855

132

- 856 [30] Liu, S., Thompson G.E., Skeldon, P. Vanadate post-treatments of anodised alu-
857 minium and AA 2024 T3 alloy for corrosion protection. *Trans. IMF* **2018** 96 137-144,
858 [DOI:10.1080/00202967.2018.1419629](https://doi.org/10.1080/00202967.2018.1419629)
- 859 [31] Brace, A.W. *The Technology of Anodizing Aluminum*, Interall S.r.l., Modena,
860 Italy, 2000
- 861 [32] Cotell, C.M., Sprague, J.A., Smidt, F.A. *ASM Handbook, Volume 5: Surface En-*
862 *gineering*. p 482-493. ASM International, Materials Park, Ohio 1994.
- 863 [33] Choi, Y.C., Hyeon, J.Y., Bu, S.D., Bae, T.S. Effects of anodizing voltages and cor-
864 responding current densities on self-ordering process of nanopores in porous anodic
865 aluminas anodized in oxalic and sulfuric acids. *J. Korean Phys. Soc* **2009** 55 835–840.
- 866 [34] Ono, S., Masuko, N. Evaluation of pore diameter of anodic porous films formed
867 on Aluminum. *Surf. Coat. Technol* **2003** 169-170 139–142.
- 868 [35] Choudhary, R.K., Mishra, P., Kain, V., Singh, K., Kumar, S., Chakravartty, J.
869 Scratch behavior of aluminum anodized in oxalic acid: Effect of anodizing potential.
870 *Surf. Coat. Technol* **2015** 283, 135–147. <https://doi.org/10.1016/j.surfcoat.2015.10.042>
- 871 [36] Martinez-Viademonte, M.; Abrahami, S.T.; Hack, T.; Burchardt, M.; Terryn, H.
872 A review on anodizing of aerospace aluminum alloys for corrosion protection. *Coat*
873 **2020** 10 1–. <https://doi.org/10.3390/coatings10111106>
- 874 [37] Bozza, A.; Giovanardi, R.; Manfredini, T.; Mattiolo, P. Pulsed current effect on
875 hard anodizing process of 7075-T6 aluminum alloy. *Surf. Coat. Technol* **2015** 270 139–
876 144. <https://doi.org/10.1016/j.surfcoat.2015.03.010>.
- 877 [38] Schaedel, F. The leading-edge guide to top quality anodizing using the com-
878 plete spectrum approach with a universal type I-II-III (123) mixed electrolyte. *Prod.*
879 *Finish* **2012** 76 9 1–13. [https://www.pfonline.com/articles/electrodepositi on-of-ni-fe-](https://www.pfonline.com/articles/electrodeposition-of-ni-ferro-ni-alloys-15th-quarterly-report)
880 [mo-w-alloys – 15th-quarterly-report](https://www.pfonline.com/articles/electrodepositi on-of-ni-fe-mo-w-alloys-15th-quarterly-report)
- 881 [39] van Put, M.A.; Abrahami, S.T.; Elisseeva, O.; de Kok, J.M.M; Mol, J.M.C.; Ter-
882 rryn, H. Potentiodynamic anodizing of aluminum alloys in Cr (VI)-free electrolytes.
883 *Surf. Interface Anal* **2016** 48 946–952. <https://doi.org/10.1002/sia.5919>
- 884 [40] O’Sullivan, J.P.; Wood, G.C. The morphology and mechanism of formation of
885 porous anodic films on aluminium. *Proceedings of the Royal Society of London, Se-*
886 *ries A, Math. Phys. Sci* **1970** 317 511 - 543.
887 <https://doi.org/10.1098/rspa.1970.0129>

135

- 888 [41] Runge, J.M.; Hossain, T. Interfacial phenomena in 7000 series alloys and their
889 impact on the anodic oxide. *Mater. Today Proc* **2015** *2* 10 5055–5062. [https://doi.org/](https://doi.org/10.1016/j.matpr.2015.10.096)
890 [10.1016/j.matpr.2015.10.096](https://doi.org/10.1016/j.matpr.2015.10.096)
- 891 [42] Davis, J.R. Introduction to Aluminum and Aluminum Alloys, ASM Interna-
892 tional, Materials Park, Ohio, 1998.
- 893 [43] ASM Handbook Committee, Properties of Wrought Aluminum and Aluminum
894 Alloys, ASM International, Materials Park, Ohio, 1990.
- 895 [44] Torrescano-Alvarez, J.; Curioni, M.; Zhou, X.; Skeldon, P. Effect of anodizing
896 conditions on the cell morphology of anodic films on AA2024-T3 alloy. *Surf. Interface*
897 *Anal* **2019** *51* 12 1135–1143. <https://doi.org/10.1002/sia.6562>
- 898 [45] H. Habazaki, H.; Shimizu, K.; Skeldon, P.; Thompson, G.; Wood, G.; Zhou, X.
899 Effects of alloying elements in anodizing of aluminium. *Trans. Inst Met. Finish* **1997** *75*
900 *1* 18–23. <https://doi.org/10.1080/00202967.1997.11871137>
- 901 [46] “Standard Test Method for Seal Quality of Anodic Coatings on Aluminum by
902 Acid Dissolution,” ASTM B680-80, in Annual Book of ASTM Standards, vol. 02.05.
903 <https://doi.org/10.1520/B0680-80R14>
- 904 [47] “Standard Test Method for Operating Salt Spray (Fog) Apparatus,” ASTM
905 B117-19, in Annual Book of ASTM Standards, vol. 03.02. [https://doi.org/10.1520/](https://doi.org/10.1520/B0117-19)
906 [B0117-19](https://doi.org/10.1520/B0117-19)
- 907 [48] Voevodin, N.N., Balbyshev, V., Donley, M. Investigation of corrosion protec-
908 tion performance of sol–gel coatings on AA2024-T3. *Progress in Organic Coatings*. **2005**
909 *52* 28–33. <https://doi.org/10.1016/j.porgcoat.2004.05.006>
- 910 [49] García-Rubio, P., Climent-Font, A., Smith, R., Curioni, M., Thompson, G., Skel-
911 don, P., Lavía, A., García, I. Influence of molybdate species on the tartaric acid/sul-
912 phuric acid anodic films grown on AA2024 T3 aerospace alloy. *Corros. Sci.* **2019** *51*
913 *2034–2042*. <https://doi.org/10.1016/j.corsci.2009.05.034>
- 914 [50] García-Rubio, Ocón, P., Curioni, M., Thompson, G. ., Skeldon, P., Lavía, A., &
915 García, I. Degradation of the corrosion resistance of anodic oxide films through im-
916 mersion in the anodising electrolyte. *Corros. Sci* **2010** *52* 2219–2227. [https://doi.org/](https://doi.org/10.1016/j.corsci.2010.03.004)
917 [10.1016/j.corsci.2010.03.004](https://doi.org/10.1016/j.corsci.2010.03.004)

138

- 918 [51] Priet, B., Odemer, G., Blanc, C., Giffard, K., & Arurault, L. Effect of new sealing
919 treatments on corrosion fatigue lifetime of anodized 2024 aluminium alloy. *Surf.*
920 *Coat. Technol.* **2016** 307 206–219. <https://doi.org/10.1016/j.surfcoat.2016.07.083>
- 921 [52] López, V., González, J.A., Otero, E., Escudero, E., Morcillo, M. Atmospheric cor-
922 rosion of bare and anodised aluminium in a wide range of environmental conditions.
923 Part II: electrochemical responses. *Surf. Coat. Technol* **2002** 153 235–244, [https://](https://doi.org/10.1016/S0257-8972(01)01681-4)
924 [doi.org/10.1016/S0257-8972\(01\)01681-4](https://doi.org/10.1016/S0257-8972(01)01681-4).
- 925 [53] Hitzig, J., Jüttner, K., Lorenz, W.J., Paatsch, W. AC-impedance measurements
926 on
927 porous aluminium oxide films. *Corros. Sci.* **1984** 24 945–952. [https://doi.org/10.](https://doi.org/10.1016/0010-938X(84)90115-X)
928 [1016/0010-938X\(84\)90115-X](https://doi.org/10.1016/0010-938X(84)90115-X).
- 929 [54] Hitzig, J., Jüttner, K., Lorenz, W.J., Paatsch, W. AC-impedance measurements
930 on
931 corroded porous aluminum oxide films. *J. Electrochem. Soc* **1986** 133 887,
932 <https://doi.org/10.1149/1.2108756>.
- 933 [55] González, J.A., López, V., Bautista, A., Otero, E., Nóvoa, X.R. Characterization
934 of
935 porous aluminium oxide films from a.c. impedance measurements. *J. Appl. Elec-*
936 *trochem.* **1992** 29 229–238, <https://doi.org/10.1023/A:1003481418291>.
- 937 [56] Boisier, G., Pébère, N., Druetz, C., Villatte, M., Suel, S. FESEM and EIS study of
938 sealed AA2024 T3 anodized in sulfuric acid electrolytes: influence of tartaric acid. *J.*
939 *Electrochem. Soc.* **2008** 155 C521. <https://doi.org/10.1149/1.2969277>.
- 940 [57] Boisier, G., Lamure, A., Pébère, N., Portail, N., Villatte, M. Corrosion protection
941 of AA2024 sealed anodic layers using the hydrophobic properties of carboxylic acids.
942 *Surf. Coat. Technol* **2009** 203 3420–3426. [https://doi.org/10.1016/J.](https://doi.org/10.1016/J.SURFCOAT.2009.05.008)
943 [SURFCOAT.2009.05.008](https://doi.org/10.1016/J.SURFCOAT.2009.05.008).
- 944 [58] Goldstein, J.I.; Newbury, D.E.; Michael, J.R.; Ritchie, N.W.M.; Scott, J.H.J.; Joy,
945 D.C. Scanning Electron Microscopy and X-Ray Microanalysis. Springer, New York,
946 2018.
- 947 [59] ImageJ, Image Processing and Analysis. <https://imagej.nih.gov/ij/>. (Accessed 15
948 March 2022).

141

949

[60] Keller, F.; Hunter, M.S.; Robinson, D.L. Structural features of oxide coatings on aluminum. *J. Electrochem. Soc* **1953** 100 411 – 419.

950

951

<https://doi.org/10.1149/1.2781142>

952

953

[61] National Institute of Standards & Technology Certificate of Analysis Standard Reference Material® 1976c Instrument Response Standard for X-Ray Powder Diffraction. <https://www-s.nist.gov/srmors/certificates/1976c.pdf>

954

955

956

[62] Walpole, R.E., Myers, R.H., Myers, S.L., Ye, K.E. Probability and Statistics for Engineers and Scientists, 9th Ed, Pearson, London, UK, 2022.

957

958

959

[63] Usman, Scenini, F., & Curioni, M. The effect of exposure conditions on performance evaluation of post-treated anodic oxides on an aerospace aluminium alloy: Comparison between salt spray and immersion testing. *Surf. Coat. Technol* **2020** 399 126157. <https://doi.org/10.1016/j.surfcoat.2020.126157>

960

961

962

[64] Newbury, D.; Ritchie, N.W. Electron-excited x-ray microanalysis by energy dispersive spectrometry at 50: analytical accuracy, precision, trace sensitivity, and quantitative compositional mapping. *Microsc. and Microanal* **2019** 25 5 1075–1105. <https://doi.org/10.1017/S143192761901482X>

963

964

965

[65] Zaidi, S.; Butt, M.; Bashir, F. A comparative study of the anodic alumina film thickness measured via SEM and evaluated using Faraday's Law. *Mater. Res. Express* **2019** 6 4 46404. <https://doi.org/10.1088/2053-1591/aafa08>

966

967

968

[66] Lee, W.; Park, S. Porous anodic aluminum oxide: anodization and templated synthesis of functional nanostructures. *Chem. Rev* **2014** 114 15 7487–7556. <https://doi.org/10.1021/cr500002z>

969

970

971

[67] Suranarayana, C.; Norton, M.G. X-ray Diffraction: A Practical Approach, Springer, New York, 1998.

972

973